A 6-year cycle in the Earth system

Julia Pfeffer, Anny Cazenave, Séverine Rosat, Lorena Moreira, Mioara Mandea, Véronique Dehant, Benjamin Coupry

Global and Planetary Change 229 (2023) 104245

Contents lists available at ScienceDirect

Global and Planetary Change

journal homepage: www.elsevier.com/locate/gloplacha

A 6-year cycle in the Earth system

Julia Pfeffer [a,*], Anny Cazenave [a,b], Séverine Rosat [c], Lorena Moreira [d], Mioara Mandea [e], Véronique Dehant [f,g], Benjamin Coupry [a]

[a] Magellium, Ramonville-Saint Agne, France
[b] LEGOS, Toulouse, France
[c] ITES, Strasbourg, France
[d] Mercator Ocean International, Toulouse, France
[e] CNES, Paris, France
[f] Royal Observatory of Belgium, Brussels, Belgium
[g] Université Catholique de Louvain, Louvain-la-Neuve, Belgium

ARTICLE INFO

Editor: Prof. Liviu Matenco

Keywords:
6-year cycle
Internal and external geodynamics
Length of day
Atmospheric angular momentum
Superficial fluid envelopes
Core
Satellite gravimetry

ABSTRACT

Oscillations with a periodicity around 6 years have long been observed in the Earth's rotation, expressed as changes in the length of day, and robustly attributed to dynamical processes in the fluid outer core pursuant to the analysis of geomagnetic data. Recently, a 6-year cycle has also been discovered in the global mean sea level changes and in some of its main contributors (i.e., mass balances of the ice sheets and glaciers). Here, we report additional observations of the 6-year cycle in the climate system. Large oscillations at periods around 6 years are detected in terrestrial water storage changes estimated from satellite gravity measurements and global hydrological models, in agreement with satellite and in-situ precipitation observations. We also find a significant 6-year cycle in the global mean Earth's surface temperature observed since the beginning of the 1980s. Finally, in agreement with previous studies, we report a 6-year cycle in the atmospheric angular momentum in opposition of phase with the length of day. As changes in the length of day are in opposition with respect to changes in the solid Earth's rotation, this suggests that the atmosphere and the solid Earth rotate together at a 6-year period, possibly in response to deep Earth's processes. These new discoveries raise the question of the links between dynamical processes occurring in the core, solid Earth and superficial fluid envelopes at the 6-year period, as well as the nature of the mechanisms driving 6-year oscillations in integrative geodetic variables, such as the length of day or gravity field.

1. Introduction

An oscillation at a period around 6 years was first reported in early measurements of the Earth's rotation, resulting in changes in the length of day (LOD) with an order of magnitude of 0.1 ms (Vondrák and Burša, 1977). The occurrence of a 6-year cycle in LOD changes (ΔLOD) was confirmed by further studies (e.g., Abarca del Rio et al., 2000; Gorshkov, 2010; Holme and de Viron, 2013; Chao et al., 2014; Duan et al., 2015; Ding, 2019; Duan and Huang, 2020; Hsu et al., 2021; Ding et al., 2021a; Rekier et al., 2022) and mainly attributed to the exchange of angular momentum between the Earth's mantle and the core, either via electromagnetic coupling at the outer core-mantle boundary (CMB) (e.g., Gillet et al., 2009, 2010) or mantle-inner core gravitational coupling (e.g., Mound and Buffett, 2003, 2006; Chao, 2017). While the exact nature of the torques at work is still debated, the observation of a 6-year cycle in the secular acceleration of the geomagnetic field (Silva et al., 2012) favours fluid core-mantle interactions. Indeed, fast core flow, expressed as torsional (Gillet et al., 2010) and Magneto-Coriolis (Gillet et al., 2022a) waves with periods peaking at 6 and 7 years respectively, were evidenced in surface core flow models inferred from geomagnetic data and found to be consistent with ΔLOD data in terms of period, phase and amplitude (Fig. 2a in Gillet et al., 2010). It has recently been shown that an important part of the 6-year LOD cycle can be attributed to core effects, after applying necessary corrections for the atmosphere, ocean and hydrology (Rosat and Gillet, 2023). Besides, oscillations at a 6-year period were also identified in geodetic observations of the polar motion, that were only partially explained by external fluid envelopes (i.e. ocean, atmosphere, hydrosphere), the rest being attributed to a deep

* Corresponding author.
E-mail address: julia.pfeffer@magellium.fr (J. Pfeffer).

https://doi.org/10.1016/j.gloplacha.2023.104245
Received 10 March 2023; Received in revised form 11 September 2023; Accepted 12 September 2023
Available online 16 September 2023

Earth source (Chen et al., 2019).

A 6-year cycle was detected in GNSS (Global Navigation Satellite System)-based observations of the Earth's equator ellipticity (Ding and Chao, 2018). A potential explanation may come from the propagation of a 6-year pressure wave in the fluid outer core forced by the inner core libration induced by mantle-inner core gravitational coupling (Ding and Chao, 2018). Such a mechanism would generate a degree 2 order 2 pattern in surface displacements and gravity field, further observed in SLR (Satellite Laser Ranging) and GRACE space gravimetry data (Chao and Yu, 2020). The analysis of >500 GNSS time series confirmed the existence of a degree 2 order 2 pattern in surface displacements at a recurring period of 6 years (Watkins et al., 2018). As surface loading from external fluid envelopes could not explain the surface displacements observed at a period of 6 years, a deeper origin was suggested, potentially associated with dynamical pressure coupling at the CMB (Watkins et al., 2018). Further analyses have questioned the significance of the 6-year cycle observed in GNSS and SLR observations considering the uncertainties on satellite geodetic measurements and models used to correct for surface loading (Rosat et al., 2021). Besides, it was pointed out that the gravity changes (Dumberry, 2010) and surface displacements (Gillet et al., 2021) expected from core processes are at least one order of magnitude smaller than the 6-year cycles observed in GNSS and SLR observations (Rosat et al., 2021; Gillet et al., 2021). If real, the 6-year oscillations observed in surface displacements and gravity field would therefore more likely be due to external sources, such as hydrological loading, rather than core dynamics (Rosat et al., 2021; Gillet et al., 2021).

A puzzling spatio-temporal correlation between the magnetic and gravity fields was observed at interannual time scales and length scales of a few thousand km and attributed to physicochemical processes at the CMB (e.g. Mandea et al., 2012, 2015). Further studies considering longer time series have shown that the common variability of the gravity field and magnetic field occurs at periods around 6 to 7 years (Dumberry and Mandea, 2022). Several statistical methods (i.e., Principal Component Analysis, Singular Value Decomposition and Multivariate Singular Spectrum Analysis) have since been applied to search for common signatures in satellite observations of the Earth's magnetic and gravity fields, also highlighting common oscillations at periods around 6 to 7 years (Saraswati et al., 2023). Different mechanisms were investigated to explain the correlation between satellite gravity and magnetic observations, including dissolution - crystallization processes of mantle silicate rocks in the liquid alloy of the outer core (Mandea et al., 2015). Such processes may indeed generate larger perturbations of the gravity field at the surface (Mandea et al., 2015) than the processes taken in consideration by Dumberry (2010) and Rosat et al. (2021), though their exact quantification remains extremely challenging.

More recently, evidence of a 6-year cycle was also found in the climate system. A periodic signal peaking around 6 to 7 years was detected in the Global Mean Sea Level (GMSL), and found to be one of the most significant period in the rate of change of the GMSL once corrected for the main climate modes, such as ENSO (El Ninõ - Southern Oscillation), PDO (Pacific Decadal Oscillation), Indian Ocean Dipole (IOD), North Atlantic Oscillation (NAO) and Atlantic Multidecadal Oscillation (AMO) (Moreira et al., 2021). Significant power was found at periods around 6 years in Multivariate ENSO Index (MEI), PDO and AMO, as well as in the mass balance of the Greenland ice sheet and glaciers and the terrestrial water storage contribution to sea level (Moreira et al., 2021). In this study, we report new observations of a 6-year cycle in the terrestrial water storage estimates based on the satellite gravity missions GRACE and GRACE-FO, consistent with precipitation and global hydrological models. We also report a 6-year cycle in the global mean Earth's surface temperature measured over the past 42 years.

The causes of such oscillations in the climate system are still unexplained, but raise the question of the relative contributions of the Earth's deep interior and external surface fluid envelopes to the 6-year cycles reported in many geodetic variables. Indeed, while some of these 6-year fluctuations are convincingly attributed to Earth's deep interior processes (e.g. for LOD), for some other variables (e.g. the gravity field), climate-related processes occurring in the surface fluid envelopes or at the Earth's surface may be more likely. Besides, oscillations occurring at the 6-year period in the Earth's deep interior and external fluid envelopes may be linked through the Earth's rotation. Indeed, we show in the present study an opposition of phase between the angular momentum of the atmosphere (AAM) and the length of day, which suggests that the Earth's mantle and the atmosphere oscillate together at a 6-year period, possibly in response to deep Earth's drivers.

An overview of the 6-year cycles observed in different variables of the Earth's system may therefore help to better understand potential links between the solid Earth and climate. In the following, we briefly review known observations of a 6-year cycle (section 2) attributed to dynamical processes in the deep Earth's interior (section 3) and surface fluid envelopes (section 4). We complete this review with new detections of a 6-year cycle in land hydrology, atmospheric water cycle and global mean surface temperature (section 4). Finally, we revisit the analysis of ΔLOD and ΔAAM, highlighting the anti-correlation between the two variables, suggesting that deep Earth's processes may have an impact on the rotation of the atmosphere and therefore on various climate parameters (section 5).

2. Observability of a 6-year cycle

The length of a time series is critical to assess the observability of a periodic signal. The Rayleigh criterion determines a minimal allowable frequency separation between two periodic constituents (e.g., tides) for a record length T (Godin, 1972):

$$|\sigma_1 - \sigma_2|\, T > R \tag{1}$$

where σ_1 and σ_2 are the frequencies of harmonic functions and R is the Rayleigh constant. For observational time series, R is usually set to 1 (Foreman and Henry, 1989). From there, one can determine the minimum and maximum periods P_{min} and P_{max} that can be separated from a period P, such as:

$$P_{min} = \frac{1}{\frac{1}{P} + \frac{1}{T}} \tag{2}$$

and

$$P_{max} = \frac{1}{\frac{1}{P} - \frac{1}{T}} \tag{3}$$

The minimum and maximum Rayleigh periods associated with a 6-year cycle are shown in Fig. 1, together with observations reported in the literature and the present study. Despite the apparent variability observed around the 6-year period, the observations are consistent with each other when the record length is considered. For example, Magneto-Coriolis waves travelling in the fluid outer core with a maximum of power peaking at 7 years could hardly be differentiated from a 6-year cycle, given the current 22-year maximal length of satellite magnetic field observations (Gillet et al., 2022a). Similarly, the length of GRACE and GRACE-FO records (~20 years at the time of writing) would not allow clearly distinguishing periodic signals in the 4.5–8.5-year period band. The spectral resolution is improved with longer sets of satellite observations such as SLR (available since the early 1990s) or the Very Long Base Interferometry (VLBI) that has provided high-accuracy Earth's orientation data since the early 1980s. The term 6-year cycle is therefore used in this study as a generic term, allowing significant dispersion around that period, especially for short observational records.

In the following, new detections of a 6-year cycle are carried out using two different approaches, namely: (i) the power spectral analysis of unfiltered time-series, and (ii) the application of a bandpass filter

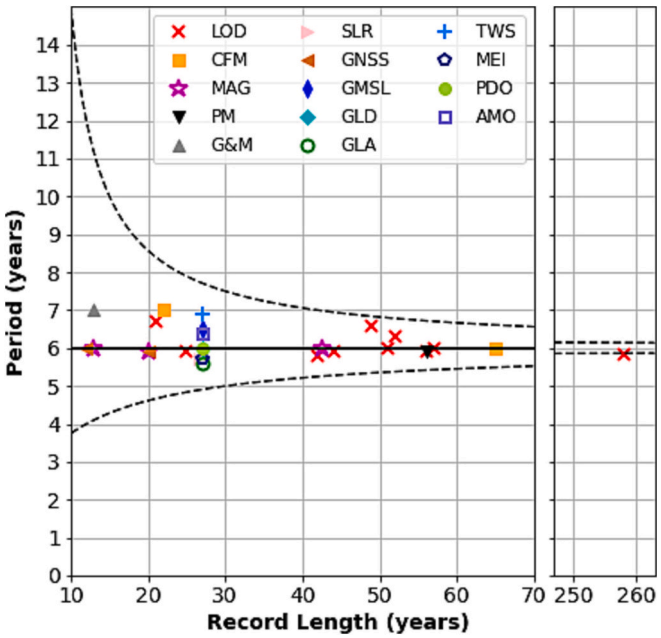

Fig. 1. Observability of a 6-year cycle depending on the length of the time series. Observations of the 6-year cycle are represented with coloured markers. The associated references are given in Appendix 1. LOD stands for Length of Day, CFM for Core Flow Models, MAG for geomagnetic data, PM for polar motion, G&M for gravity and magnetic data, SLR for Satellite Laser Ranging, GNSS for Global Navigation Satellite System, GMSL for Global Mean Sea Level, GLD for Greenland, GLA for glaciers, TWS for Terrestrial water Storage, MEI for Multivariate ENSO Index, PDO for Pacific Decadal Oscillation and AMO for Atlantic Multidecadal Oscillation. Warm colours (red, maroon, orange, pink, magenta, black, grey) indicate observations associated with the solid Earth and Earth's interior, while cold colours (blue, green) indicate climate observations. Dashed lines indicate the minimum and maximum periods that can be separated from a 6-year period using the Rayleigh criterion. (For interpretation of the references to colour in this figure legend, the reader is referred to the web version of this article.)

adapted to the record length. Both tools serve different purposes. The power spectral analysis is useful to demonstrate the occurrence of a 6-year cycle in the presence of autocorrelated noise. The band-pass filter allows the extraction of the 6-yr cycle to better characterise its phase, amplitude and spatial distribution.

2.1. Detection of a 6-year cycle with a power spectral analysis

The power spectral density (PSD) of individual time series is determined with the Lomb-Scargle periodogram (VanderPlas, 2018). Before calculating the PSD, the time series are systematically detrended and deseasoned by least squares adjustment of a linear trend, annual sinusoid and semi-annual sinusoid. Unless explicitly stated otherwise, the PSD is always calculated for unfiltered time series. The only exception concerns precipitation time series, for which we apply a lowpass filter with a cutoff period of 1 year to remove high frequency noise. The statistical significance of the detected peaks is evaluated for an autocorrelated noise model (also known as red noise), using a Monte Carlo approach (e.g. Schulz and Mudelsee, 2002). For each observation record $\boldsymbol{x}(t)$, we generate 15,000 realisations of a red noise model $\boldsymbol{y}(t)$, as:

$$y(t) = r_1 . y(t-1) + \epsilon \tag{4}$$

where $\boldsymbol{y}(t)$ is the value of the red noise model at time $\boldsymbol{t}$, $\boldsymbol{r_1}$ is the autocorrelation coefficient of lag 1 and $\boldsymbol{\epsilon}$ is a random number drawn from a standardised normal distribution (i.e. white noise model characterised by a uniform power spectrum). The autocorrelation coefficient r_1 is calculated from the observed time series $\boldsymbol{x}(t)$ as:

$$r_1 = \frac{\sum_{t=1}^{N-1}(x_t - \bar{x})(x_{t+1} - \bar{x})}{\sum_{t=1}^{N}(x_t - \bar{x})^2} \tag{5}$$

The PSD of each red noise model is normalised so that its total energy equals the total energy of the observed time series, calculated as the integral of the PSD. The confidence levels at 95%, 90% and 85% are calculated as the 95th, 90th and 85th percentiles of the 15,000 PSDs of red noise models. If a peak in the PSD of the observed time series $\boldsymbol{x}(t)$ is above the 95% confidence level (CL), it means that there is <5% chance to be only due to red noise.

2.2. Extraction of the 6-year cycle with a bandpass filter

Once robustly detected with a power spectral analysis or with other methods such as MSSA (Multivariate Singular Spectrum Analysis, e.g. Ghil et al., 2002), the 6-year cycle may be extracted from a time series using a bandpass filter. Here, we use a classical butterworth filter of order 5, designed to flatten the frequency response in the passband. The cutoff periods are calculated as the minimum and maximum Rayleigh periods (Eq. 2 and 3), so that the passband is consistent with the spectral resolution associated with the record length.

3. A 6-year cycle in the deep Earth's interior

Satellite and ground observations of the magnetic field are the primary source of information on the dynamical processes originating in the Earth's core at time scales ranging from a couple of years to slightly more than a century (Lesur et al., 2022). Time-dependent geomagnetic field models, such as the KALMAG (Baerenzung et al., 2020), CHAOS7 (Finlay et al., 2020) or COV-OBS.x2 (Huder et al., 2020), constitute excellent tools to explore such temporal changes, as they combine measurements collected from ground observatories and satellites (CHAMP, Swarm, CryoSat-2, SAC—C, Oersted) and allow the separation of internal and external sources in the geomagnetic field. Here, we show evidence of a 6-year cycle in the main EOF (Empirical Orthogonal Functions; see North, 1984 for a mathematical description of EOFs) component of the secular acceleration of the radial component of the magnetic field, explaining about 30% of the total variance (Fig. 2). The peak in the PSD of the principal component of the secular acceleration of the magnetic field, with an exact period estimated at 6.6 years, is well above the 95% CL (Fig. 2b). Other oscillations were identified in the second, third, fourth and fifth components of CHAOS7 radial secular acceleration with considerable power at interannual and decadal time scales (not shown). Such results are consistent with previous observations indicating significant changes in the magnetic field at interannual and decadal time-scales (Lesur et al., 2022), with a maximum of power around 6-years (Silva et al., 2012; Gillet et al., 2010, 2022a,b). To the best of our knowledge, it is the first time that the 6-year cycle is identified as the dominant component of the secular acceleration of the magnetic field. Previous studies either focused on shorter and sparser observations (e.g., Silva et al., 2012), or on specific waves detected in core flow models (e.g., Gillet et al., 2010, 2022a,b).

Torsional waves (associated with differentially rotating geostrophic cylinders) have been considered in an ensemble of core flow models for explaining independent ΔLOD observations with a period around 6 years both in terms of phase and amplitude (Gillet et al., 2010, 2022a, 2022b; Gerick et al., 2021). The magnetic signature attributed to torsional waves was shown to be too weak to entirely explain SV changes, suggesting the existence of other types of waves in the fluid outer core (Gillet et al., 2015; Cox et al., 2016; Aubert, 2018), such as QG (quasi-geostrophic) Alfven waves, QG Magneto-Coriolis (MC) waves or Magnetic- Archimedes-Coriolis (MAC) waves (e.g., Pais and Jault, 2008; Gillet et al., 2022b). A recent study suggests that both torsional Alfven waves and QG MC waves can contribute to interannual ΔLOD

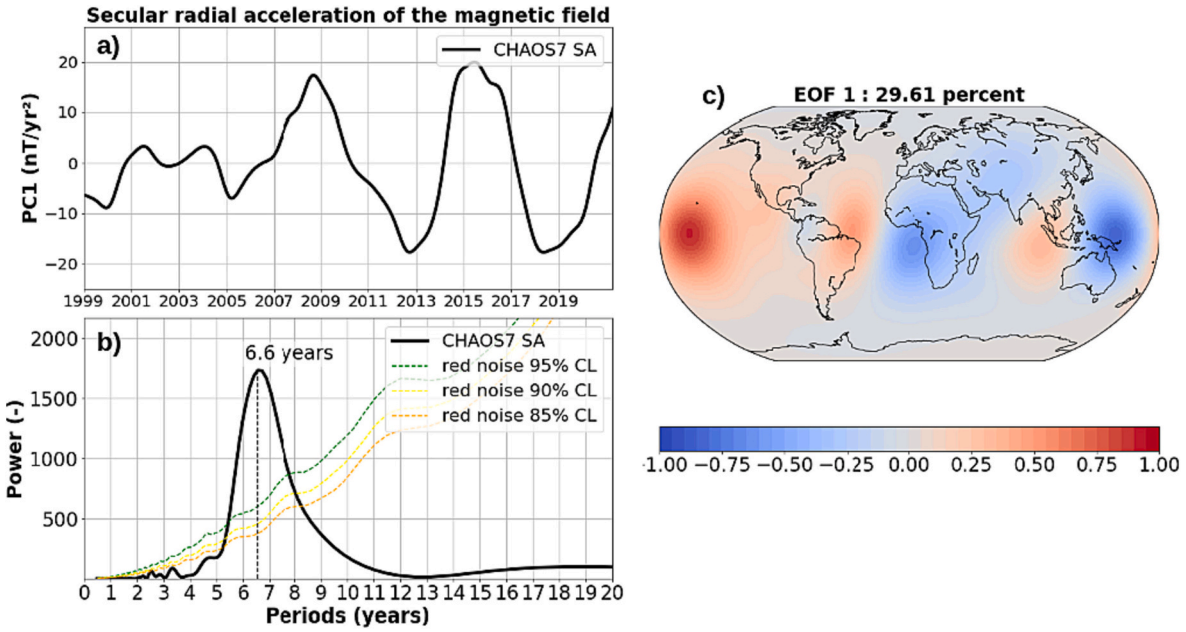

Fig. 2. Principal component (a) of the EOF decomposition of the secular acceleration of the radial component of the magnetic field modelled with CHAOS7, with its associated PSD (b) and spatial pattern (c). The 95%, 90% and 85% CL are indicated as green, yellow and orange hatched lines in (b). (For interpretation of the references to colour in this figure legend, the reader is referred to the web version of this article.)

observations at periods around 6 and 8.5 years (Istas et al., 2023). This was confirmed by Rosat and Gillet (2023) using a wavelet coherence analysis. These authors also showed that higher-frequency oscillations at 3.5 and 5-years could be a QG MC waves signature. One should however remain cautious in this interpretation, as a significant part of the patterns observed in the magnetic field are still not well resolved by core flow models (Lesur et al., 2022).

Dynamical processes in the fluid outer core observed in the magnetic field may in turn generate changes in the Earth's gravity field, through (i) pressure variations at the CMB or (ii) density heterogeneities in the fluid outer core and (iii) changes in the rotation of the inner core (e.g. Dumberry, 2010; Dumberry and Mandea, 2022). Because such processes

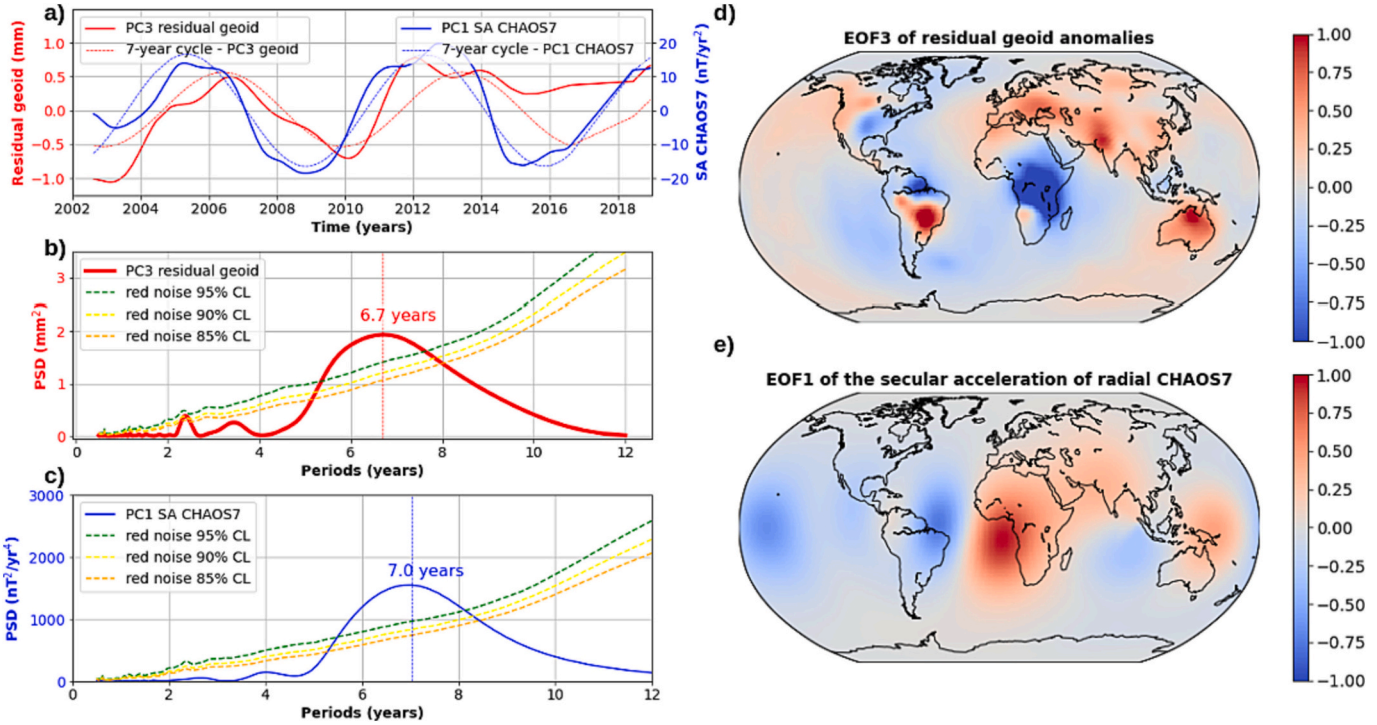

Fig. 3. (a) Comparison of the principal component of the secular acceleration of the radial component of the magnetic field modelled with CHAOS7 with the third component of the geoid anomalies estimated with GRACE and GRACE-FO observations corrected for glacial isostatic adjustment, hydrology and ocean-atmosphere circulation. (b) Power Spectral densities associated with the third component of residual geoid anomalies. (c) Power Spectral Densities associated with the principal component of the secular acceleration of the magnetic field. (d) Spatial pattern (EOF) associated with the PC3 of residual geoid anomalies. (e) Spatial pattern (EOF) associated with the PC1 of the secular acceleration of the radial component of the geomagnetic field.

would generate changes in the gravity field below the level of uncertainty of satellite measurements (e.g., Dumberry, 2010; Rosat et al., 2021; Lecomte et al., 2023), other processes should be proposed to explain the common variability of the magnetic and gravity field at periods around 6 to 7 years (e.g. Dumberry and Mandea, 2022; Saraswati et al., 2023). Such processes could either be related to internal or external geodynamics.

We revisit here the comparison of the correlated signals observed in the magnetic and gravity fields using an EOF decomposition. A 7-year oscillation is detected in the first and third components of the secular acceleration of the geomagnetic field and geoid anomalies corrected for surface processes respectively (Fig. 3). Both oscillations are well above the 95% CL (Fig. 3). The geoid data are based on the ensemble mean of nine GRACE and GRACE-FO solutions, including 3 mascons solutions (i.e. CSR, JPL, GSFC) and 6 spherical harmonic solutions (i.e. JPL, CSR, GFZ, ITSG, CNES, COST-G) with consistent corrections applied for the geocenter, C20, C30, GIA, ocean-atmosphere circulation and land hydrology (see Appendix 2 and Pfeffer et al., 2023 for details). The record length is limited by the period of overlap (2002–2018) between GRACE and GRACE-FO measurements (2002 - present day) and the hydrological model ISBA-CTRIP (1979–2018). The 17 years of the record length is not sufficient to discriminate 6-year from 7-year periodic oscillations (Fig. 1). A moderate correlation (Pearson correlation coefficient R = 0.45) is found between the temporal components of CHAOS7 secular acceleration and the geoid anomalies, and a clear phase shift (~ 1 year) is observed in the 7-year cycles of both components (Fig. 3).

The spatial patterns of the EOF decomposition of the magnetic and geoid data (Fig. 3) are very dissimilar and do not display any significant spatial correlation (R = -0.15). The secular acceleration of the magnetic field displays a strong dipole centred on the South Atlantic, with a negative anomaly over South America and a positive anomaly across Central Africa (Fig. 3). In the geoid spatial pattern, the 7-year oscillation is particularly visible over large river basins, such as Central Africa (Congo basin), North of South America (Amazon and Sao Francisco basins), North of Australia and North of India (Fig. 3). Similar spatial patterns are not necessarily expected in the magnetic and gravity field, even if generated by a common deep Earth's source (Saraswati et al., 2023). However, the 7-yr oscillations in the residual geoid anomalies are essentially located in hydrologically active areas, which points towards superficial rather than a deep Earth's source. Here, the geoid anomalies have been corrected for land hydrology using the ISBA-CTRIP modelling system (Decharme et al., 2019). However, global hydrological models tend to underestimate Terrestrial Water Storage (TWS) changes on interannual and decadal time-scales, likely due to insufficient constraints on the groundwater cycle (Pfeffer et al., 2023). While we cannot exclude a deep Earth's origin for the common temporal geomagnetic and gravity signals, as suggested by Mandea et al. (2012, 2015), the 7-year oscillation in GRACE and GRACE-FO observations likely reflects hydrological processes poorly resolved by global hydrological models, thus still present in the corrected geoid data. We investigate this issue in more detail in section 4.

4. A 6-year cycle in the Earth's external fluid envelopes

4.1. Evidence of a 6-year cycle in land hydrology and precipitation

In this section, we present new evidence of a 6-year cycle in GRACE and GRACE-FO estimates of terrestrial water storage changes, consistent with in-situ (GPCC, Schneider et al., 2014) and satellite-based (IMERG, Huffman et al., 2019) precipitation records and predictions from two global hydrological models (ISBA-CTRIP, Decharme et al., 2019, and WGHM, (Cáceres et al., 2020; see Pfeffer et al., 2023 for a description of both models). In order to extract a 6-year cycle, we apply a band-pass filter on the time-series using complete record lengths and the Rayleigh criterion to determine cutoff-periods (Appendix 2). Mapping the amplitude of the 6-year cycle (Fig. 4) allows highlighting 13 regions of interest (Fig. 5), where further spectral analyses are carried out on unfiltered time series (Fig. 6 and 7).

The precipitation strongly oscillates at a 6-year period along the equator and within the tropics (Fig. 4a). Large oscillations are also detected in the terrestrial water storage changes estimated both from GRACE (Fig. 4b) and global hydrological models (Fig. 4c and d) in tropical regions, especially in the Southern Hemisphere (Amazon and Congo basins, and South-East Asia). Significant amplitude of the 6-year

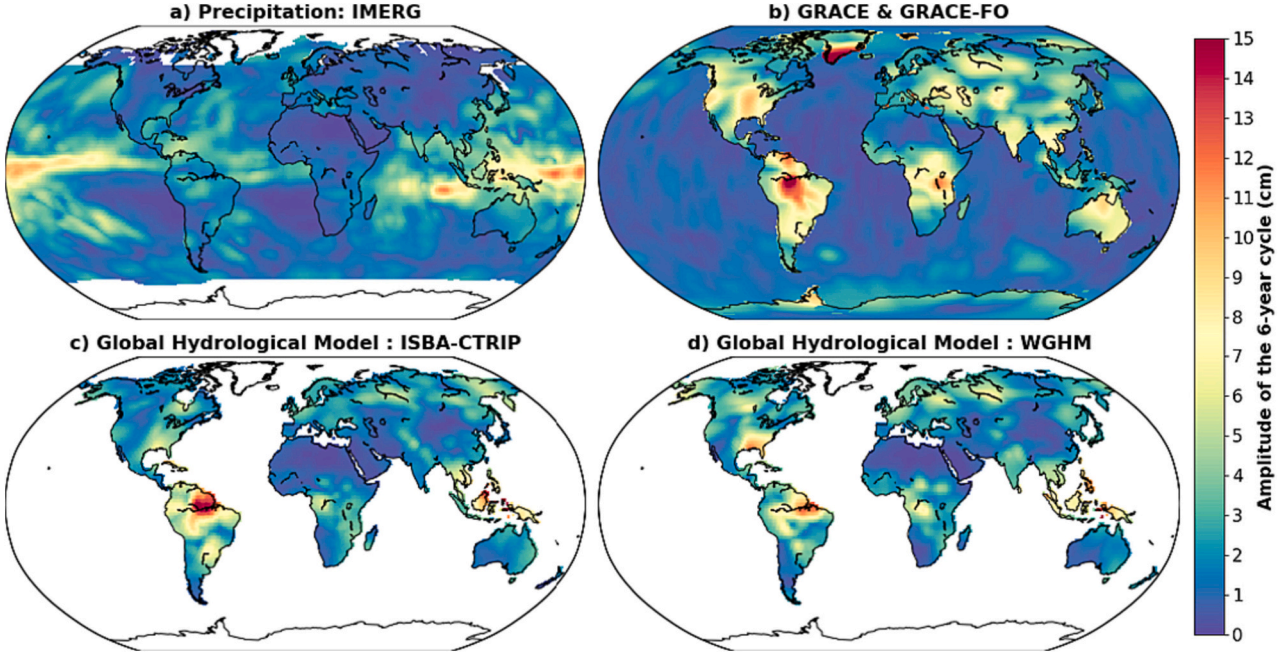

Fig. 4. Amplitude of the 6-year cycle in precipitation (a) and terrestrial water storage changes estimated with GRACE and GRACE-FO (b) and two global hydrological models ISBA-TRIP (c) and WGHM (d). The amplitude of the 6-year cycle is calculated as the difference between the maximum and minimum of the bandpass filtered signal, using the Rayleigh criterion to determine cutoff periods.

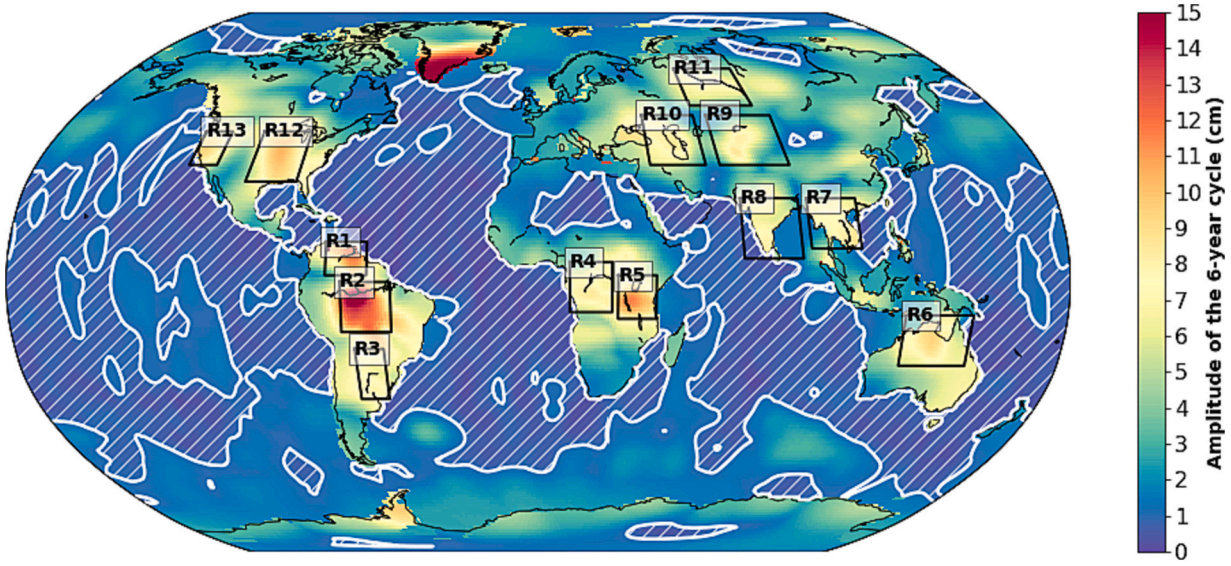

Fig. 5. Regions displaying large oscillations in the 4.6–8.6 years waveband in GRACE and GRACE-FO TWS estimates. The white hatched areas correspond to regions where the amplitude of the 6-year cycle is below 1 cm, which is twice the maximum noise level estimated in the 4.6–8.6 years waveband (see Appendix 3).

cycle is also observed in the terrestrial water storage in North America (especially in the Mississippi River basin), Siberia (Ob and Yenisei river basins) and around the Caspian Sea (GRACE and GRACE-FO data only). Overall, the amplitude of the 6-year cycle is stronger in GRACE and GRACE-FO than in the global hydrological models. This may be due to an underestimation of interannual TWS changes by global hydrological models, as shown in Pfeffer et al. (2023).

The noise level in GRACE and GRACE-FO has been estimated to be around 2 cm when considering the full spectral content of the nine solutions of the ensemble (see Appendix 3), which is consistent with previous studies (e.g., Chen et al., 2022). The noise level drops to 0.5 mm in the 4.6–8.6 period band (Appendix 3), so that most of the patterns evidenced in hydrologically active regions can be considered significant (Fig. 5). Here, we analyse the TWS changes in 13 regions where the amplitude of the 6-year cycle is found to be particularly large ($>$ 6 cm). We focus on regions shown to display a strong continental water cycle and a significant 6-year oscillation (Fig. 5). Extremely large amplitudes of the 6-year cycle are also observed in ice mass changes across the South of Greenland, Svalbard, Alaska and West Antarctic Peninsula (Fig. 5), in agreement with previous studies (Moreira et al., 2021).

For example over the Congo region (Fig. 6), a strong oscillation is observed with a period around 6 years in precipitation, characterised by a large peak in the PSD ranging from 5 to 8 years with a maximum at 5.5 years. The peak at 5.5 years in the PSD is significant at 90% CL (Fig. 6b). A lowpass filter with a cutoff period of 1-year was applied to remove the high-frequency noise in the precipitation. The low-pass filter increases the auto-correlation in the time series and therefore heightens the threshold associated with a given confidence level in the PSD, defined as the percentile of an ensemble of red noise models (see section 2.1). As a consequence, the 5.5-year peak exhibits higher statistical significance for unfiltered (97.5% CL) than low-pass filtered (90% CL) precipitation time series. However, a red noise model is not adapted to render the random nature of precipitation at short time scales in unfiltered time series. The application of a lowpass filter alleviates this limitation by removing the high frequency noise, allowing a more robust evaluation of the statistical significance of low frequencies in precipitation records. The 6-year oscillation is also observed in the unfiltered TWS changes estimated from GRACE (maximum of the PSD at 5.9 years with a 99.9% CL). The occurrence of a 6-year cycle is confirmed in longer global hydrological models TWS predictions from ISBA-CTRIP (PSD maximum at 6.5 years with 81.5% CL) and WGHM (PSD maximum at 6.6 years with 99.2% CL). The amplitude of the 6-year cycle is however smaller in global hydrological models than in GRACE, leaving large residuals in GRACE measurements when corrected for hydrology. The global hydrological models considered here may underestimate not only the 6-year cycle, but also most of the TWS variability at interannual and decadal time scales (Pfeffer et al., 2023). This bias is generally more acute for WGHM than ISBA-CTRIP (Fig. 6 and 7; Appendix 4; Pfeffer et al., 2023).

The same analyses have been carried out on all selected regions (Fig. 5) and confirm the systematic occurrence of a 6-year cycle in precipitation, TWS changes and TWS residuals (see all power spectral analyses in Appendix 4 and their synthesis in Fig. 7). The closest peaks to a 6-year period that were detected in the PSD of hydrological time series were reported in Fig. 7. The periods of the detected peaks are consistent with the spectral resolution of the observation records and lie within the minimum and maximum Rayleigh periods framing the 6-year cycle for all regions, except for R11 (Ob River, Fig. 7i). Most periods lie within 5 and 7 years, except for three peaks at 4.0, 4.7 and 4.8 years detected in R11 (Ob River), R5 (Great African Lakes) and R8 (India). The statistical significance of the detected peaks is generally higher for longer records such as GPCC and ISBA-CTRIP, exhibiting CL above 80% for all regions except R3 (Parana River) and R5 (Great African Lakes). For R3 (Parana river), low CL ($<$80%) are also reached for GRACE-based and WGHM-based TWS anomalies, indicating a weak probability of the occurrence of a 6-year cycle in this region. On the other hand, significant oscillations are detected around 6 years with GRACE (87.9% CL) and WGHM (94.2% CL) in the Great African Lakes region (R5). A 6-year cycle may therefore occur in this region in processes other than precipitation, which may not be adequately captured by GPCC or ISBA-CTRIP. Across the Amazon (R2), the 6-year cycle is significant in all observations (89.1% CL for precipitation, 87.2% CL for ISBA-CTRIP and 91.8% CL for WGMH) except GRACE (62.3% CL). The GRACE and GRACE-FO observation period may simply be too short to be able to discriminate a 6-year cycle from autocorrelated noise in the Amazon region (R2).

While detected both by GRACE and global hydrological models (Fig. 7c, e and g), the amplitude of the 6-yr cycles is generally underestimated by global hydrological models when compared to GRACE (Fig. 4), leaving large residuals in TWS changes at a 6-year period (Fig. 6 and Appendix 4). Unresolved hydrological processes in the models (e.g., likely in the groundwater compartment; see Pfeffer et al., 2023 for a discussion) therefore necessarily lead to significant residual geoid anomalies at periods of 6 to 7 years (Fig. 3). Considering the large contributions from hydrology (up to a few 10 cm) and significant

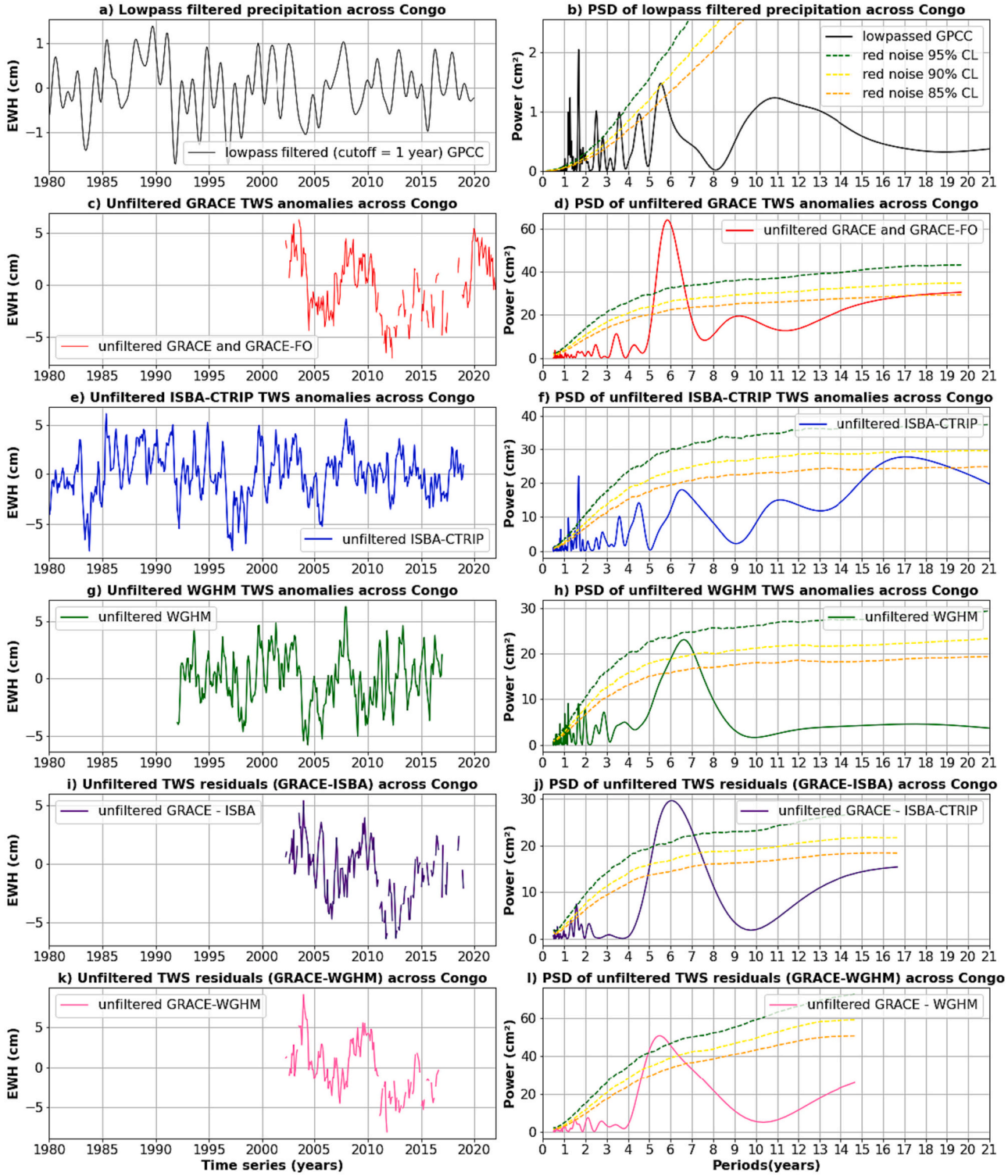

Fig. 6. Comparison of precipitation and TWS anomalies averaged over the Congo region (R4 in Fig. 5). The power spectral densities (PSD) are shown for unfiltered time series, except for precipitation where a lowpass filter is applied with a cutoff period of 1 year. The confidence levels at 85, 90 and 95% are shown as orange, yellow and green hatched lines. a) Low-pass filtered (cutoff period = 1 year) precipitation anomalies estimated with the gauge-based GPCC product. (b) PSD of the lowpass filtered (cutoff period = 1 year) precipitation anomalies. (c) Unfiltered TWS anomalies estimated with GRACE and GRACE-FO. (d) PSD of the unfiltered TWS anomalies estimated with GRACE and GRACE-FO. (e) Unfiltered TWS anomalies predicted with ISBA-CTRIP. (f) PSD of the unfiltered TWS anomalies predicted by ISBA-CTRIP. g) Unfiltered TWS anomalies predicted with WGHM. h) PSD of the unfiltered TWS anomalies predicted by WGHM. i) Unfiltered TWS residuals calculated as the difference between GRACE and ISBA-CTRIP. j) PSD of unfiltered TWS residuals calculated as the difference between GRACE and ISBA-CTRIP. k) Unfiltered TWS residuals calculated as the difference between GRACE and WGHM. l) PSD of the unfiltered TWS residuals calculated as the difference between GRACE and WGHM. (For interpretation of the references to colour in this figure legend, the reader is referred to the web version of this article.)

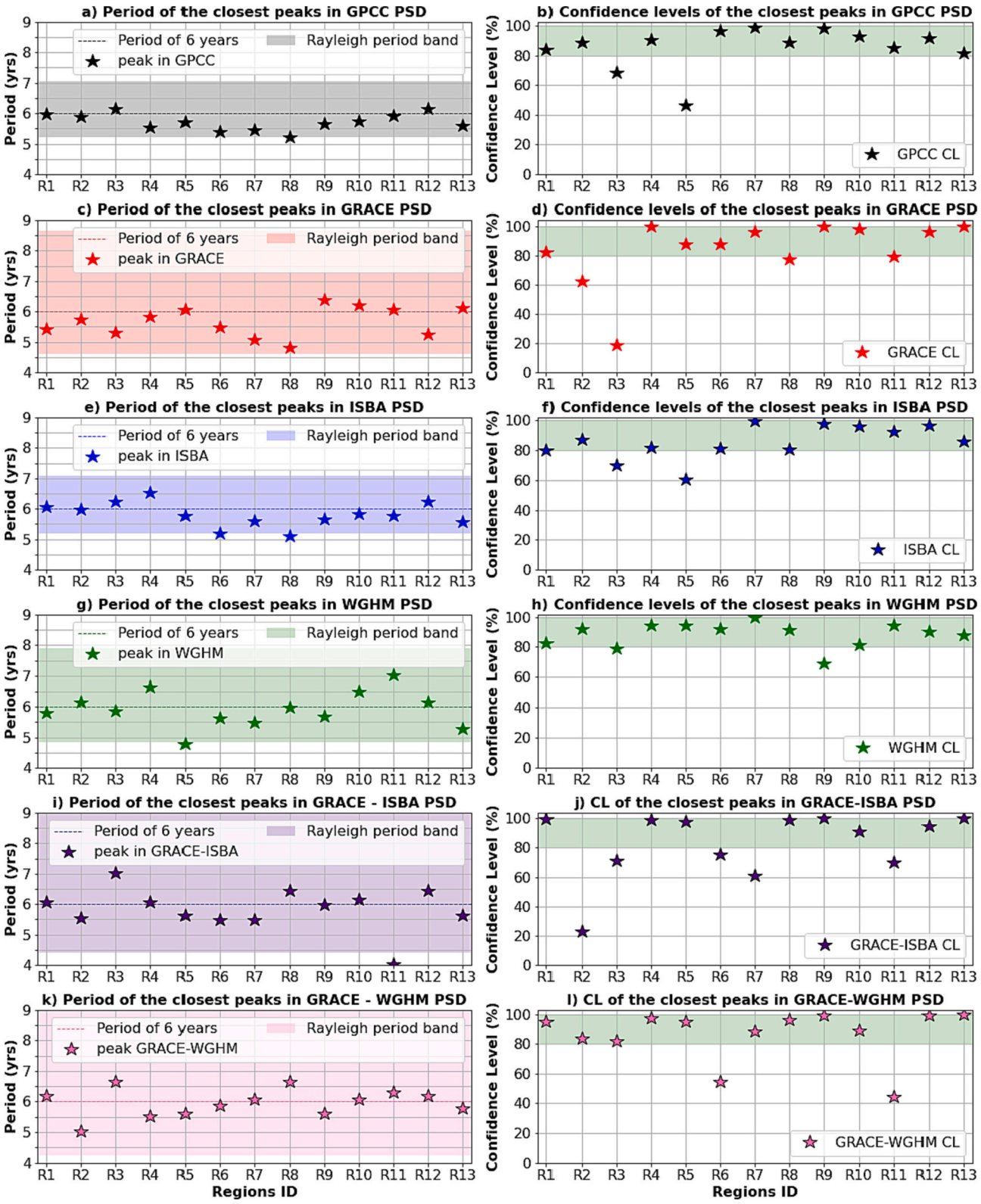

Fig. 7. Closest peaks to a 6-year cycle and associated confidence levels (CL) detected in the power spectral density (PSD) of GPCC precipitation (a,b), GRACE TWS anomalies (c,d), ISBA TWS anomalies (e,f), WGHM TWS anomalies (g,h), GRACE-ISBA TWS residuals (i,j), GRACE-WGHM (*k*,*l*) across 13 selected regions (see Fig. 5).

uncertainties in global hydrological models (up to a few cm) at inter-annual and decadal time scales (e.g. Pfeffer et al., 2023), the extraction of subcentimetric signals expected from the core (0.5 cm in Lecomte et al., 2023) in satellite gravity data still remains a difficult and challenging task.

4.2. *Evidence of a 6-year cycle in other climate parameters*

Significant oscillations at periods ranging from 6 to 7 years were discovered in the global mean sea level (GMSL) changes monitored by satellite altimetry and corrected for the interannual variability

associated with internal climate modes, such as ENSO and PDO. Significant oscillations at a period of 6 to 7 years were also evidenced in the main contributions to the GMSL, in particular in the rate of change of the ice mass balances of glaciers and Greenland (Moreira et al., 2021). Besides, significant energy was found around 6 years in several natural climate modes, namely MEI, PDO and AMO. As climate indices are defined by the statistical analysis of several combined atmospheric and oceanic variables (e.g., atmospheric pressure, sea surface temperature, surface winds, etc.), it indicates significant contributions of the 6-year cycle in several climate variables. For example, a ~ 7 cycle was reported in the European land surface temperature (Jajcay et al., 2016; Meyer and Kantz, 2019), possibly related to NAO.

Here we also report the occurrence of a 7.1-year cycle at 95% CL in the global mean surface temperature (GMST) observed from January 1980 to December 2022 (Fig. 8). A linear trend, annual sinusoid and semi-annual sinusoid were removed from the HadCRUT5 GMST data (Morice et al., 2021). According to the Rayleigh criterion, a 7.1-year periodic oscillation cannot be differentiated from 6.1 to 8.5-year oscillations for a 43-year long record. Therefore, the 7.1 year oscillation detected in the GMST remains broadly consistent with the generic definition of a 6-year cycle given in section 2 (Fig. 1). However, significant dispersion exists around the 6-year oscillation, especially in the climate system, as noted previously by Moreira et al. (2021).

5. Links between the deep Earth's interior and climate system

Oscillations have been detected at periods around 6 years in the Earth's interior and in the climate system. Both may be unrelated and may incidentally occur with similar periodicities. However, one could also imagine a link from the solid Earth and the superficial fluid envelopes through the Earth's rotation. The conservation of angular momentum of the whole Earth's system requires that fluctuations in the angular momentum in one of the Earth's envelopes be compensated by equal but opposite fluctuations in the rest of the system.

At seasonal periods, changes in the AAM (ΔAAM) caused by zonal wind circulation are responsible for ΔLOD, as a result from the transfer of angular momentum from the atmosphere to the Earth's mantle via frictional, topographic and gravitational torques at the air-solid surface interface (Munk and MacDonald, 1960; Lambeck, 1980; Barnes et al., 1983). Transfer of angular momentum from the atmosphere to the solid Earth has also been associated with ENSO at interannual time scales (e.g., Chao, 1989; De Viron and Dickey, 2014; Gross et al., 1996). At seasonal and interannual time scales, the ocean circulation and the global water cycle also contribute ΔLOD variations but the contributions of the oceanic and hydrospheric angular momenta – OAM and HAM, respectively) are smaller than the AAM by about one order of magnitude for OAM and 3 to 4 times for HAM (e.g. Chen et al., 2000; Chen, 2005; Rosat and Gillet, 2023). At multidecadal and longer time scales, ΔLOD are dominated by tidal frictions, mass redistributions in the Earth's interior (including GIA) and angular momentum exchange between the core and

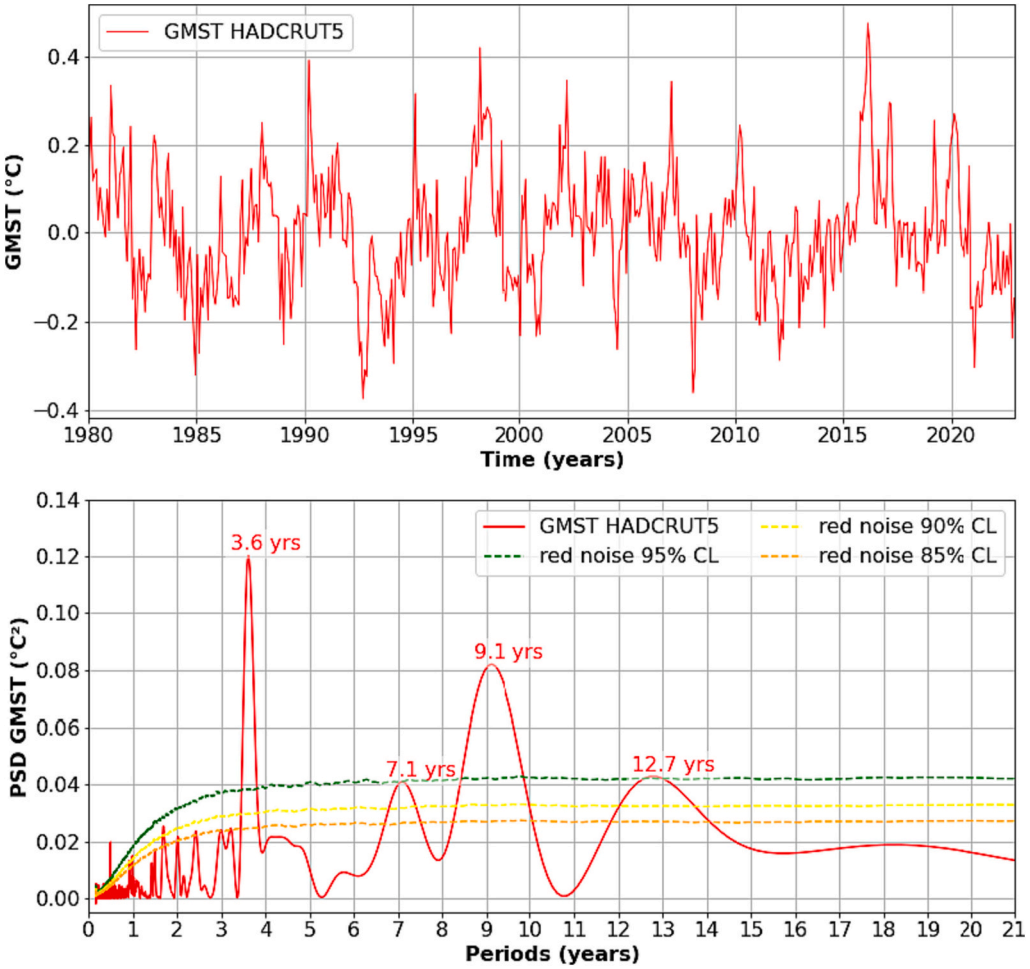

Fig. 8. a) Variations of the HadCRUT5 global mean surface temperature (GMST) over January 1980–December 2022 with a linear trend, annual sinusoid and semi-annual sinusoid removed. b) PSD of detrended and deseasoned HADCRUT5 GMST. The confidence levels at 85, 90 and 95% are shown as orange, yellow and green hatched lines. (For interpretation of the references to colour in this figure legend, the reader is referred to the web version of this article.)

mantle (Jault et al., 1988; Hide et al., 1993; Buffett, 1996; Mound and Buffett, 2006; Rekier et al., 2022). At interannual time scales, ΔLOD have been more difficult to interpret as the excitations originated from the deep Earth's interior and the superficial fluid envelopes overlap. The 6-year cycle in ΔLOD can however not be explained by the exchange of angular momentum with superficial fluid envelopes (e.g., Abarca del Rio et al., 2000, 2012). Indeed, correcting ΔLOD for ΔAAM, ΔOAM and ΔHAM does not cancel the 6-year cycle in ΔLOD (Chen et al., 2019; Rekier et al., 2022), but on the contrary enhances it, unlike at seasonal and ENSO frequencies where cancellation is well observed. This clearly strengthens the assumption of a core origin (e.g., Mound and Buffett, 2003, 2006; Gillet et al., 2010; Holme and de Viron, 2013; Gillet et al., 2022a; Istas et al., 2023; Rosat and Gillet, 2023).

Here, we revisit the analysis of the 6-year cycle in ΔLOD and ΔAAM. ΔLOD time series are the EOP C04 combined series (Bizouard et al., 2019) corrected for tides provided by the IERS (International Earth Rotation and Reference Systems Service) including observations from four space geodetic systems (VLBI, SLR, GPS, DORIS). ΔAAM time series are calculated as the sum of the mass (using the inverted barometer assumption) and motion terms of the effective atmospheric angular momentum functions as calculated from NCEP/NCAR reanalyses (Salstein et al., 1993, Salstein and Rosen, 1997and Salstein et al., 2005; Zhou et al., 2006). The radial ΔAAM (in $kg.m^2.s^{-1}$) are converted to ΔLOD (in s) according to Eubanks et al. (1985):

$$\Delta LOD = \frac{LOD}{\omega_0 I}\Delta AAM \tag{6}$$

where LOD is 86,400 s, ω_0 is the mean rotation rate of the Earth (7.29×10^{-5} s^{-1}) and I is the axial moment of inertia of the solid Earth, including the mantle and crust ($7.04 \times 10^{37} kg\ m^2$). A scale factor of $1.68 \times 10^{-29}\ s^2.kg^{-1}.m^{-2}$ is therefore applied to ΔAAM in order to get ΔLOD associated with the atmosphere contribution. For legibility, the atmospheric contribution to ΔLOD is simply referred to as ΔAAM in the following. Both ΔLOD and ΔAAM time series are extracted over the January 1980–December 2021 time period, when high quality data are available. Seasonal signals and linear trends are removed from the time series using the outputs of a least square adjustment of a linear trend, annual sinusoid, semi-annual sinusoid and constant terms.

The power spectral analysis of ΔLOD, ΔAAM and their residuals confirms that ΔLOD is dominated by decadal and pluri-decadal periods, while ΔAAM exhibits large variability at interannual time scales, with significant (> 95% CL) peaks in the PSD at 2.4, 3.7 and 5.5 years (Fig. 9). The ΔLOD residuals (difference between ΔLOD and ΔAAM) are corrected for high frequencies (including the 2.4 and 3.7 periods corresponding to ENSO), except for the 5.6 period (> 85% CL), which is enhanced in the residuals compared to the original ΔLOD data. This result is consistent with Chen et al. (2019) and Rekier et al. (2022). The present analysis clearly shows the occurrence of a 6-year cycle in ΔAAM, with a 99.4% CL when considering red noise. The exact period is estimated at 5.5 years, which cannot be distinguished from a 6-year period given the record length. It may be noted that our red noise model fits the full energy of the observed time series. Such assumption is not realistic for ΔLOD observations that are dominated by low frequencies, and results in the underestimation of the statistical significance of peaks at higher frequencies. The application of a high-pass filter may alleviate that limitation. The statistical significance of the 6-yr cycle is indeed increased in ΔLOD (82.9% CL) after application of a high-pass filter with a cutoff period of 8 years.

A vast number of studies (many listed in section 1, Fig. 1 and Appendix 1) demonstrates the occurrence of a 6-yr cycle in ΔLOD, and a few more (Chen et al., 2019; Rekier et al., 2022; Rosat and Gillet, 2023) highlight the fact that the 6-yr cycle is enhanced in ΔLOD residuals corrected for external fluid envelopes (including ΔAAM, ΔOAM and ΔHAM). In agreement with Chen et al. (2019); Rekier et al. (2022) and Rosat and Gillet (2023), this study reports the occurrence of a 6-year cycle in ΔAAM. To better characterise the phase and amplitude of the 6-year cycle, a bandpass filter is applied on ΔLOD, ΔAAM and their residuals with cutoff periods calculated using the Rayleigh criterion (P_{min} = 5.23 years and P_{max} = 7.03 years).

The semi-amplitude of the 6-year cycle reaches ~0.1 ms for ΔLOD and ~ 0.15 ms for ΔAAM (Fig. 10). The amplitude of the 6-year cycle in

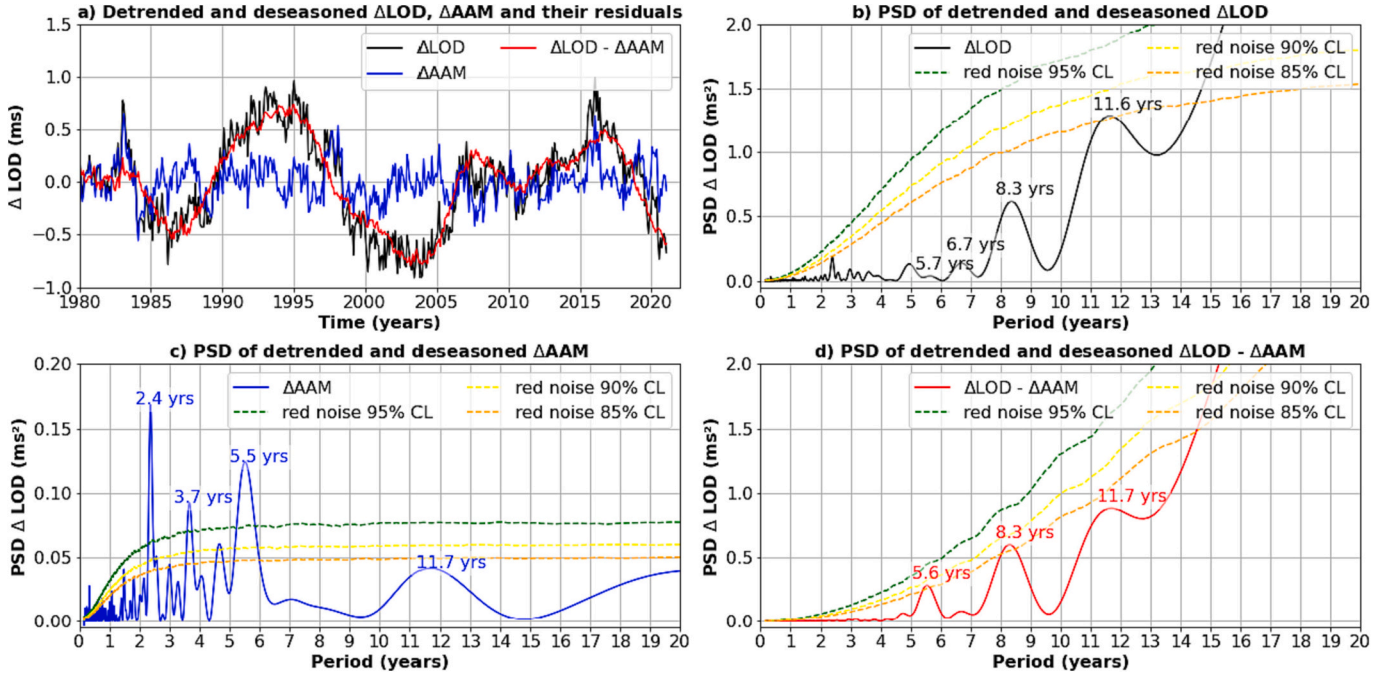

Fig. 9. a) Variations in the length of day (ΔLOD), Atmospheric Angular Momentum (ΔAAM) and their residuals (RES = ΔLOD-ΔAAM) over January 1980–December 2020 with a linear trend, annual sinusoid and semi-annual sinusoid removed. PSD of detrended and deseasoned ΔLOD (b), ΔAAM (c) and ΔLOD residuals corrected for ΔAAM (d). The confidence levels at 85, 90 and 95% are shown as orange, yellow and green hatched lines. (For interpretation of the references to colour in this figure legend, the reader is referred to the web version of this article.)

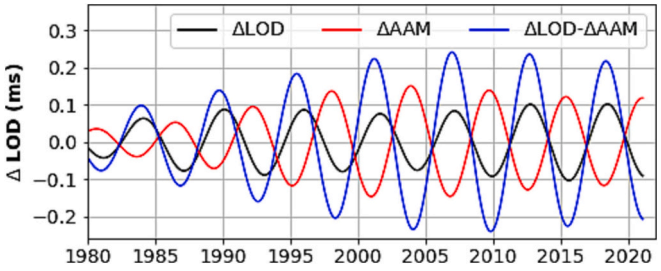

Fig. 10. Variations in the length of day filtered between 5.23 and 7.03 years. The cutoff periods of the bandpass filtered have been calculated to extract a 6-year periodic signal from 41-year records using the Rayleigh criterion. The observed ΔLOD time series (EOP C04 combined series) are shown in black, the contribution from the atmosphere (NCEP reanalysis) in red, and the difference in blue. (For interpretation of the references to colour in this figure legend, the reader is referred to the web version of this article.)

ΔAAM is noticeably larger than reported in Chen et al. (2019) (~0.04 ms in Table 3). There might be several explanations for such differences. First, the length of the time series considered is different (1962–2018 for Chen et al., 2019), which may have a significant impact on the amplitude of the estimated signals. Second, the techniques used to isolate the 6-yr cycle are different which may also generate some differences in the amplitude. In particular, in Chen et al. (2019) the isolated periods are between 2 and 8 years in their Fig. 9; this accounts thus for several contributions of the atmosphere at other periods than 6 years. Finally, Chen et al. (2019) or Rekier et al. (2022) focus on the sum of angular momentum from the atmosphere, ocean and hydrosphere (AOH). Since the HAM is slightly out of phase with AAM at a 6-yr period, it may reduce the amplitude of the AOH signal. There might indeed be a delay between the 6-yr cycle in the AAM and the response of climate parameters, especially for land hydrology (specific basin responses, groundwater responses etc.).

A striking opposition of phase can be observed between the ΔLOD and ΔAAM (Fig. 10), expressed by a strong anti-correlation between the two time series (R = -0.79). As a result, when correcting the observed ΔLOD for the atmospheric contribution, the 6-year cycle is enhanced (PSD maximum at 5.8 years, semi-amplitude ~0.2 ms), as noticed previously by Chen et al. (2019) and Rekier et al. (2022).

However, none of these previous studies suggested an explanation for the phase opposition between the ΔLOD and ΔAAM. Because the solid Earth's rotational rate is in phase opposition with ΔLOD, the opposition of phase between ΔLOD and ΔAAM means that the atmosphere and solid Earth rotate together at a 6-year period. The situation is therefore very different for the 6-year cycle than for seasonal or ENSO time scales. At ENSO and seasonal time scales, the atmosphere excites the solid Earth, through the generation of a torque, leading to ΔLOD and ΔAAM signals that are in phase. At a 6-year period, the atmosphere does not excite the solid Earth, but simply rotates with it, possibly in response to an excitation from the core. Indeed, assuming that the 6-year cycle detected in ΔLOD originates from dynamical processes in the core, which is supported by numerous geomagnetic observations and core flow models, the same processes would be responsible for the rotation of the atmosphere. Processes originating in the deep Earth's interior would therefore affect the rotation of the solid Earth and the atmosphere as a single system. The exact nature of the coupling mechanism between the atmosphere and the solid Earth is not known yet.

The AAM is a fundamental index describing the global atmospheric circulation, and therefore climate variability (e.g., Egger et al., 2007). A strong relationship has been found between ΔAAM and various climate modes such as ENSO (e.g., Dickey et al., 1992; Rosen et al., 1984), NAO (e.g., Chao and Zhou, 1998; De Viron et al., 2001) and MJO (Madden-Julian Oscillation) (e.g., Weickmann and Sardeshmukh, 1994), indicating changes in the climate system as a whole (wind circulation, sea surface temperatures, precipitation, surface pressure etc.). A 6-year cycle in the ΔAAM, impulsed by the deep Earth's processes via the rotation of the solid Earth, may therefore generate oscillations at similar periods in the whole climate system, including the wind circulation, cloud cover, temperature, precipitation and in turn land hydrology. While direct effects of masses redistribution in the Earth's core may be too small to be detected by GRACE measurements (e.g., Rosat et al., 2021; Dumberry and Mandea, 2022; Lecomte et al., 2023), indirect effects related to the exchange of angular momentum between the core, the solid Earth and the atmosphere may have a larger impact on the gravity field via atmospheric, oceanic and hydrological surface loading variations. The observations listed in the present study demonstrate the occurrence of a 6-year cycle in many environmental variables, including the ΔAAM. Further studies are needed to better understand the nature of the coupling mechanisms linking changes in the rotation of the solid Earth and the atmosphere, hence inferred changes in the atmospheric circulation and climate. However, the collection of observations of a 6-year cycle detected in the various envelopes of the Earth's system raises new questions on the relationships between the dynamics of the deep Earth's interior and its external fluid envelopes that deserve further attention.

6. Conclusions

In this study, we have reported new evidence of oscillations in the climate system at periods around 6 years. Significant changes in the gravity field are observed in the 4.6 to 8.6 year period band with GRACE and GRACE-FO measurements, closely linked with precipitation and terrestrial water storage changes. The oscillations in terrestrial water storage are particularly large at periods around 6 years in the tropical Southern hemisphere (North of South America, central Africa, North Australia) and tropical Northern hemisphere (Indian Peninsula, South-East Asia), but are also found at higher latitudes (Central Valley, Mississippi basin, Caspian Sea, central Asia, Ob basin). These observations echo the recent discovery of a 6-year cycle in the rate of change of the global mean sea level and some of its main contributors, including the ice mass balances of Greenland and continental glaciers (Moreira et al., 2021). We also show here new detection of a 6-year cycle in the Earth's global mean surface temperature (GMST).

The existence of a 6-year cycle in ΔLOD has long been known and robustly attributed to dynamical processes in the fluid outer core, which is supported by satellite and in situ observations of the geomagnetic field and subsequent core flow models. While our findings tend to confirm such results, we also highlight an opposition of phase between ΔLOD (an opposite measure of the solid Earth rotation rate) and ΔAAM at the 6-year period. We suggest that the anti-correlation between the ΔLOD and ΔAAM indicates a coupled oscillation of the solid Earth and the atmosphere in response to dynamical processes that originated in the Earth's outer core. The mechanisms required to induce a coupling between the core, the solid Earth and the atmosphere are not yet understood. However, oscillations in the ΔAAM at periods around 6-years are indubitably present in atmospheric reanalyses, which necessarily imply changes in the atmospheric circulation and the climate system. The changes observed in terrestrial water storage, global mean sea level and ice-mass distributions may therefore be part of a 6-year cycle in the whole climate system expressed by global and regional changes of many variables, including mean sea level, ice mass balances, precipitation, terrestrial water storage, surface temperatures and climate indices. Superficial fluid layers (i.e. ocean, atmosphere, hydrosphere) have always been treated as external forcing sources through an angular momentum approach or through torques computation. We suggest here that the Earth's may need to be analysed as a single coupled system.

Potential links between the internal Earth's dynamics and climate may also occur at longer (i.e., multidecadal) timescales. Oscillations in the magnetic field have been observed at periods around 60 to 70 years (e.g., Currie, 1973; Roberts et al., 2007; Jackson and Mound, 2010; Dobrica et al., 2018) and attributed to dynamical processes in the fluid

outer core, possibly involving MAC waves (e.g., Buffett, 2014; Buffett et al., 2016). Similar oscillations have been observed in the Earth's rotation at periods around 60 to 65 years, as well as 20 years (Zotov et al., 2016; Marcus, 2016). While variations in the Earth's rotation around 20 years are likely partly related to the 18.6-year tidal cycle, the 60 to 65-year oscillations may have a deeper origin (Roberts et al., 2007). A recent study based on the analysis of seismic travel paths suggests that the inner core oscillates at a ~ 65-year period (Yang and Song, 2023). The oscillation of the inner core may induce changes in the geomagnetic field and length of day at similar periods through electromagnetic coupling with the outer core and gravitational coupling with the mantle (Yang and Song, 2023). Other studies have reported oscillations around 60–65 years in the climate system, e.g., in the Earth's global mean surface temperature (Schlesinger and Ramankutty, 1994), regional and global mean sea level (Chambers et al., 2012; Ding et al., 2021b), rainfall and river discharge (Enfield et al., 2001) and several climate indices, in particular AMO. These observations suggest that at multidecadal time scales, deep Earth dynamics and climate may be linked. It is interesting to note that the relationships between climate parameters, ΔLOD and the geomagnetic field at time scales of 60 to 70 years are similar to what is observed for the 6-year cycle. Climate parameters tend to be positively correlated with the Earth's mantle rotation, so negatively correlated with ΔLOD, which can be explained with core flow models inferred from geomagnetic data. Multidisciplinary work is urgently required to better understand how the different components of the Earth system, from the core to the surface, are coupled together.

Declaration of Competing Interest

The authors declare the following financial interests/personal relationships which may be considered as potential competing interests: Julia Pfeffer reports financial support was provided by European Research Council. Veronique Dehant reports was provided by Fund for Scientific Research.

Data availability

Data will be made available on request.

Acknowledgements

This project has received funding from the European Research Council (ERC) under the European Union's Horizon 2020 research and innovation program (GRACEFUL Synergy Grant agreement No 855677). The FRS-FNRS is acknowledged for the support for the Research Project (PDR No T.0066.20) on which VD was also working. The authors thank Michaël Ablain and Anne Barnoud for useful discussions about spectral analyses.

Appendix 1: Compilation of observations of a 6-year cycle

Table A1

Periods (P) and record length (T) of the 6-year cycles detected in the Length Of Day (LOD), Polar Motions (PM), Core Flow Models (CFM), geomagnetic data (MAG), gravity and magnetic data (G&M), Satellite Laser Ranging (SLR), Global Navigation Satellite System (GNSS), Multivariate ENSO Index (MEI), Pacific Decadal Oscillation (PDO), Atlantic Multi-decadal Oscillation (AMO), ice-mass balances from Greenland (GLD) and glaciers (GLA) and terrestrial water storage (TWS).

Observations	P	T	Reference	Doi
LOD	6.7	21	Vondrák and Burša, 1977	doi:https://doi.org/10.1007/BF01634821
LOD	6.6	49	Abarca del Rio et al., 2000	doi:https://doi.org/10.1007/s00585-000-0347-9
LOD	6.3	52	Gorshkov, 2010	doi:https://doi.org/10.1134/S003809461006002X
LOD	6	51	Chao et al., 2014	doi:https://doi.org/10.1111/ter.12094
LOD	5.85	258	Ding, 2019	doi:https://doi.org/10.1016/j.epsl.2018.12.003
LOD	6	57	Duan and Huang, 2020	doi:https://doi.org/10.1038/s41467-020-16,109-8
LOD	5.9	44	Rekier et al., 2022	doi:https://doi.org/10.1007/s10712-021-09669-x
LOD	5.9	56	Chen et al., 2019	doi:https://doi.org/10.1029/2019JB018541
LOD	5.8	42	Mound and Buffett, 2006	doi:https://doi.org/10.1016/j.epsl.2006.01.043
LOD	5.9	25	Ding and Chao, 2018	doi:https://doi.org/10.1016/j.epsl.2018.05.009
PM	5.9	56	Chen et al., 2019	doi:https://doi.org/10.1029/2019JB018541
CFM	6	65	Gillet et al., 2010	doi:https://doi.org/10.1038/nature09010
CFM	7	22	Gillet et al., 2022a	doi:https://doi.org/10.1073/pnas.2115258119
MAG	6	42.5	Silva et al., 2012	doi:https://doi.org/10.1029/2012JB009405
MAG	6	13	Silva et al., 2012	doi:https://doi.org/10.1029/2012JB009405
MAG	5.9	20	Ding and Chao, 2018	doi:https://doi.org/10.1016/j.epsl.2018.05.009
G&M	7	13	Mandea et al., 2020	doi:https://doi.org/10.3390/rs12244186
SLR	5.7	26.7	Chao and Yu, 2020	doi:https://doi.org/10.1016/j.epsl.2020.116316
GNSS	5.9	20	Ding and Chao, 2018	doi:https://doi.org/10.1016/j.epsl.2018.05.009
GNSS	6	12	Watkins et al., 2018	doi:https://doi.org/10.1038/s41598-018-32,043-8
GMSL	6.5	27	Moreira et al., 2021	doi:https://doi.org/10.1016/j.gloplacha.2021.103450
MEI	5.7	27	Moreira et al., 2021	doi:https://doi.org/10.1016/j.gloplacha.2021.103450
PDO	6	27	Moreira et al., 2021	doi:https://doi.org/10.1016/j.gloplacha.2021.103450
AMO	6.4	27	Moreira et al., 2021	doi:https://doi.org/10.1016/j.gloplacha.2021.103450
GLD	6	27	Moreira et al., 2021	doi:https://doi.org/10.1016/j.gloplacha.2021.103450
GLA	5.6	27	Moreira et al., 2021	doi:https://doi.org/10.1016/j.gloplacha.2021.103450
TWS	6.9	27	Moreira et al., 2021	doi:https://doi.org/10.1016/j.gloplacha.2021.103450

Appendix 2: Data processing

Geoid anomalies and changes in total terrestrial water storage (TWS) have been estimated with satellite gravimetry using the latest release of three mascon solutions from the JPL (RL06 Version 02, Wiese et al., 2019), CSR (RL06 V02; Save et al., 2016 and Save, 2020) and GSFC (RL06 V01, Loomis et al., 2019a) and six solutions based on spherical harmonic coefficients of the gravitational potential from the JPL (RL06, Yuan, 2019; GRACE-FO, 2022a), CSR (RL06, Yuan, 2019; GRACE-FO, 2022b), GFZ (RL06, Dahle et al., 2018), ITSG (GRACE2018, Mayer-Gürr et al., 2018), COST-G (RL01, Meyer et al., 2020) and CNES-GRGS (RL05, Lemoine and Bourgogne, 2020). The same corrections for the geocenter (Sun et al., 2016), C20 coefficients

(Loomis et al., 2019b) and GIA (ICE6G-D by Peltier et al., 2018) have been applied for mascon and spherical harmonic solutions. The Stokes coefficients from the JPL, CSR, GFZ, ITSG, COST-G and CNES-GRGS solutions, with the aforementioned corrections applied, have been truncated at degree 60. Spherical harmonic solutions have been converted to surface mass anomalies expressed as equivalent water height using the locally spherical approximation (Ditmar, 2018) implemented in the l3py python package (Akvas, 2018). Systematic errors (i.e., stripes) have been removed from spherical harmonic solutions (except for the constrained CNES-GRGS solutions) using an anisotropic filter based on the principle of diffusion (Goux et al., 2023), using Daley length scales of 200 and 300 km in the North-South and East-West directions, and a shape of Matern function close to a Gaussian (8 iterations). Functions from the Matern class, commonly used to characterise stochastic processes, have a shape that may vary between a decaying exponential and a Gaussian depending on the parameterization used (see Goux et al., 2023 for a complete mathematical description of the filter). The diffusive filter allows the implementation of mathematical boundaries, preventing fluxes between two spatial domains. We chose here to place a boundary at the coast to prevent leakage from the continents to the oceans (and vice versa) during the filtering step. The mascons solutions have been corrected for the atmosphere - ocean circulation, by removing the GAD of the AOD1B (Atmosphere-Ocean-Dealiasing 1B) RL07 model (Dobslaw et al., 2017), which was restored in the original datasets. The GAD product allows estimating the combined effect of the atmospheric and oceanic circulations over the oceans and is null over the continents (Dobslaw et al., 2017). To be consistent, the GAD has not been restored in spherical harmonic solutions. All nine solutions have therefore been corrected in the same manner for ocean-atmosphere circulation.

In section 3, the nine GRACE and GRACE-FO solutions have been averaged together and then corrected for land hydrology using the ISBA-CTRIP (Interaction Soil Biosphere Atmosphere - CNRM (Centre National de Recherches Météorologiques) version of Total Runoff Integrating Pathways) global land surface modelling system (Decharme et al., 2019), filtered at 250 km to be consistent with the resolution of GRACE measurements. Residual GRACE and GRACE-FO data have therefore been corrected for GIA (ICE6G-D model), ocean atmosphere circulation (AOD1B) and land hydrology ISBA-CTRIP (ISBA-CTRIP). To further correct for surface processes, ice-sheets and regions impacted by large earthquakes (Sumatra, Tohoku, Maule with using geographical limits by (Tang et al., 2020) have been masked out of the dataset. Decadal trends and seasonal signals are removed using simultaneous least square adjustment of a linear trend, annual sinusoid and semi-annual sinusoid. The residual equivalent water height anomalies have then been converted back to geopotential coefficients and geoid anomalies using the locally spherical approximation by (Ditmar, 2018). The radial component of the secular acceleration of CHAOS7 has been sampled at GRACE and GRACE-FO times and a linear trend has been removed to allow a meaningful comparison with residual GRACE and GRACE-FO data. The length of the time series (17 years) is limited by the first GRACE data (April 2002) and the latest ISBA-CTRIP TWS predictions (December 2018).

In section 4, we use the ensemble mean of the nine GRACE and GRACE-FO solutions expressed in equivalent water heights over the period April 2002–April 2022. We do not correct GRACE and GRACE-FO data for hydrology. Besides, we use two precipitation datasets based on in-situ gauges (GPCC: Schneider et al., 2014) and combined satellite measurements (IMERG; Huffman et al., 2019). The GPCC dataset covers January 1980–December 2020 and IMERG May 2000–August 2021. We also use the TWS predictions from two global hydrological models: ISBA-CTRIP and WGHM (Watergap Global Hydrological Model, Müller Schmied et al., 2021) covering the periods Jan. 1980 - Dec. 2018 and Jan. 1992 - Dec. 2016 respectively. We remove decadal trends and seasonal signals by least square adjustment of a linear trend, annual sinusoid and semi-annual sinusoid at the grid cell level in all datasets. We apply an isotropic 250-km diffusive filter on all datasets to homogenise the spatial resolution of the different products. Finally, we apply band-pass filters to extract 6-years oscillations, whose cutoff periods are determined using the Rayleigh criterion (see Eq. 2 and 3 in the main text, section 2). We deliberately choose to maximise the length of the time series to gain in spectral resolution, even if the periods selected do not match. The record length selected and associated cutoff periods are given in Table A2.

Table A2
List of products analysed in section 4.

Dataset	Record Length (years)	First month of the time series	Last month of the time series	Minimum cutoff period (years)	Maximum cutoff period (years)
GRACE & GRACE-FO	20	April 2002	April 2022	4.60	8.63
GPCC	40	January 1980	December 2019	5.22	7.06
IMERG	21.25	May 2000	August 2021	4.68	8.36
ISBA-CTRIP	39	January 1980	December 2018	5.20	7.09
WGHM	25	January 1992	December 2016	4.83	7.90

Appendix 3: Noise level in GRACE and GRACE-FO solutions

The noise level in GRACE and GRACE-FO solutions is often estimated as the RMS of detrended and deseasoned solutions over the ocean far from the coast. Very little geophysical signal is expected in this area, so that it constitutes a good indicator of the noise level in the solution. All necessary corrections (geocenter, C20, C30, GIA, dealiasing, diffusive filter, removal of linear trend, annual sinusoid and semi-annual sinusoid) are applied to the solutions as described in Appendix 2. We estimate the RMS before and after application of the bandpass filter to evaluate the noise level with the full spectral content and over the 4.6–8.6 period band only (Fig. A3). The median noise level before application of the bandpass filter is about 1.1 cm (considering the full ensemble of 9 solutions). The noise level is 1.8 cm at the 95th percentile, and 3.1 cm at the 99th percentile. Percentiles indicate the number of values of an ensemble at or below a given percentage. For example, the median can be defined as the value at the 50th percentile. After application of the band-pass filter, the noise level drops significantly, which is expected given its high-frequency nature, characterised by large spikes for individual months (e.g., February 2015). The median noise level on the bandpass filtered solutions is 2.5 mm considering the full ensemble of 9 solutions. The noise level goes up to 4.6 mm at the 95th percentile and 5.3 mm at the 99th percentile for the full ensemble of bandpassed solutions.

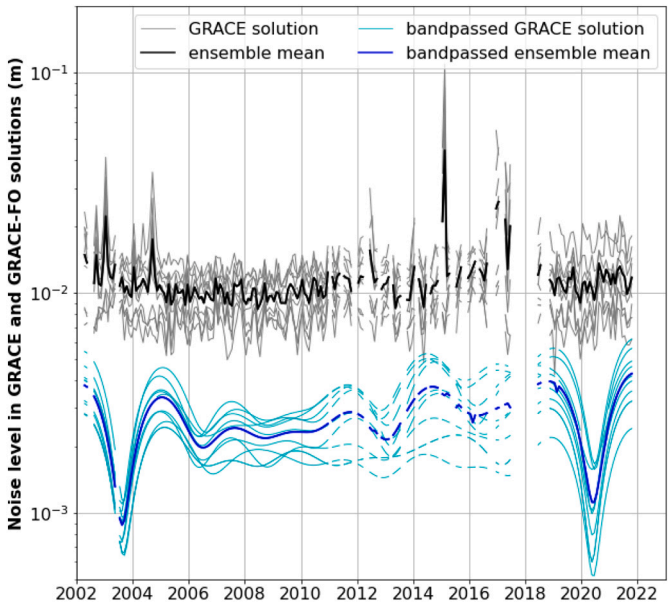

Fig. A3. Noise level in GRACE and GRACE-FO solutions estimated as the RMS over the ocean far (> 500 km) from the coast. Thin grey lines indicate the noise level for individual solutions described in Appendix 2, before applying the band-pass filter. The bold black line indicates the noise level in the ensemble mean. The noise level is also estimated in bandpass filtered solutions (cyan) and ensemble mean (blue). (For interpretation of the references to colour in this figure legend, the reader is referred to the web version of this article.)

Appendix 4: Spectral analyses of precipitation and TWS records

Large (> 6 cm) oscillations in TWS have been detected with GRACE and GRACE-FO missions in the 4.6–8.6 period band over 13 regions of the world (Fig. 5, in the main text). The power spectral analyses of unfiltered time series are shown for the Congo (R4) region in the main text (Fig. 6). We show here the spectral analyses carried out for the 12 remaining regions, including the Orinoco (R1), Amazon (R2), Parana (R3), Great African Lakes (R5), North Australia (R6), South East Asia (R7), Indian Peninsula (R8), central Asia (R9), Caspian Sea (R10), Ob (R11), Mississippi (R12) and Central Valley (R13). For each of these 12 regions, significant oscillations are systematically detected in the same period band in precipitation and TWS predictions from global hydrological models. The amplitude of TWS changes is generally underestimated by both global hydrological models when compared to GRACE in the 4.6–8.6 period band. The underestimation is more pronounced with WGHM than ISBA-CTRIP. These results are not limited to the 4.6–8.6 period band, but can be generalised to interannual and decadal time scales (Pfeffer et al., 2023). The 6-year oscillations detected in residual GRACE and GRACE-FO measurements are therefore very likely due to hydrological processes not resolved by the global hydrological models ISBA-CTRIP and WGHM. The geographical coordinates of the 13 selected regions are given in Table A4.1.

Table A4.1
Geographical coordinates of the 13 regions selected in Fig. 5.

Region	Minimum latitude	Maximum latitude	Minimum longitude	Maximum longitude
R1: Orinoco	2°N	12°N	72°W	58°W
R2: Amazon	15°S	0°S	67°W	50°W
R3: Parana	35°S	20°S	63°W	53°W
R4: Congo	9°S	6°N	11°E	25°E
R5: Great African Lakes	11°S	2°N	27°E	40°E
R6: North Australia	25°S	10°S	125°E	148°E
R7: South East Asia	10°N	25°N	93°E	110°E
R8: Indian Peninsula	7°N	25°N	70°E	90°E
R9: central Asia	35°N	50°N	65°E	90°E
R10: Caspian Sea	35°N	50°N	40°E	60°E
R11: Ob River	53°N	65°N	60°E	85°E
R12: Mississippi	30°N	45°N	103°W	85°W
R13: Central Valley	35°W	45°N	125°W	115°W

Full power spectral analyses are presented for all regions in FigA4.1 to Fig A4.12. The spectral analysis of the Congo region (R4) is presented in the main text.

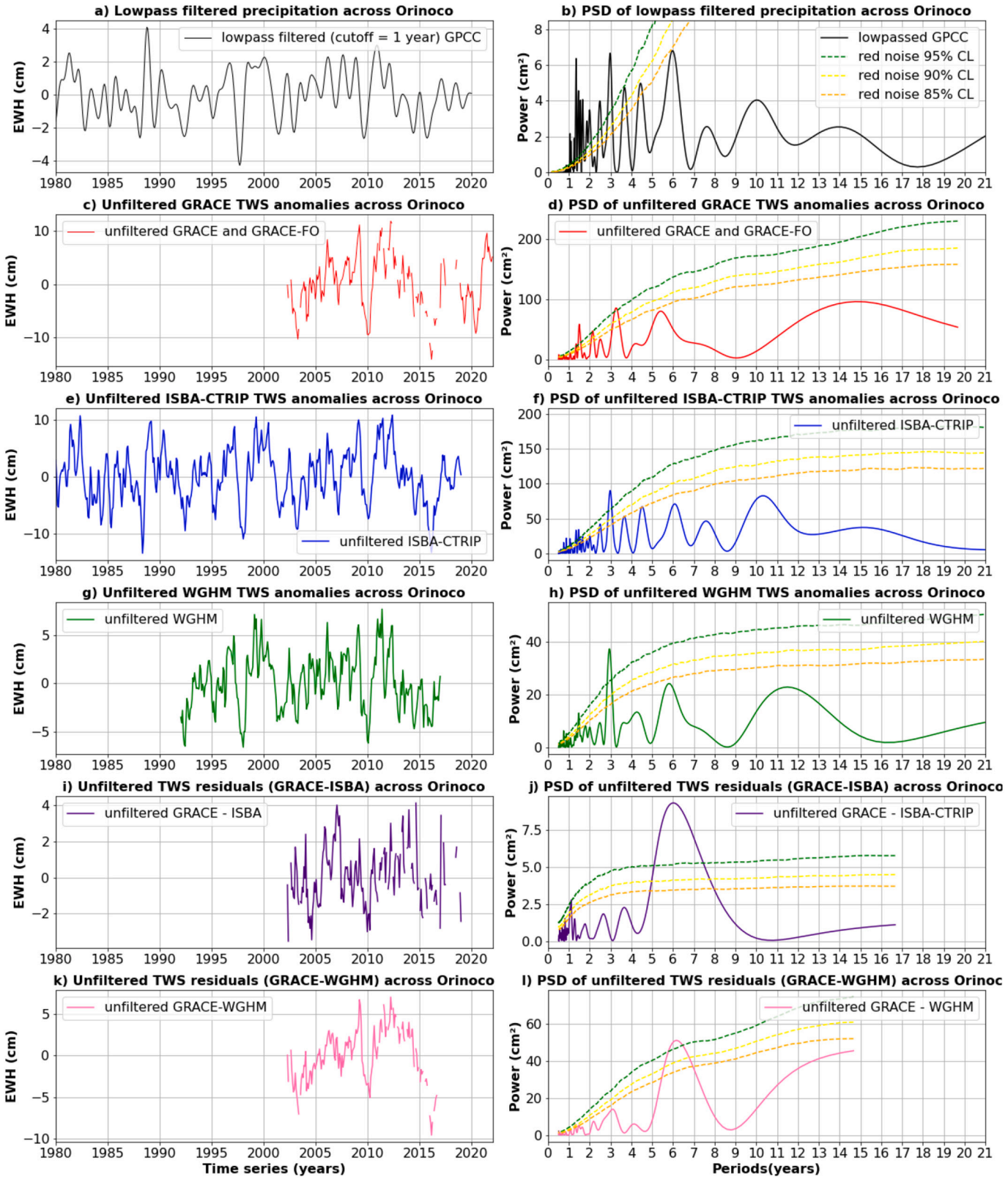

Fig. A4.1. Comparison of precipitation and TWS anomalies over the Orinoco region (region R1 in Fig. 5). The layout is the same as for Fig. 6.

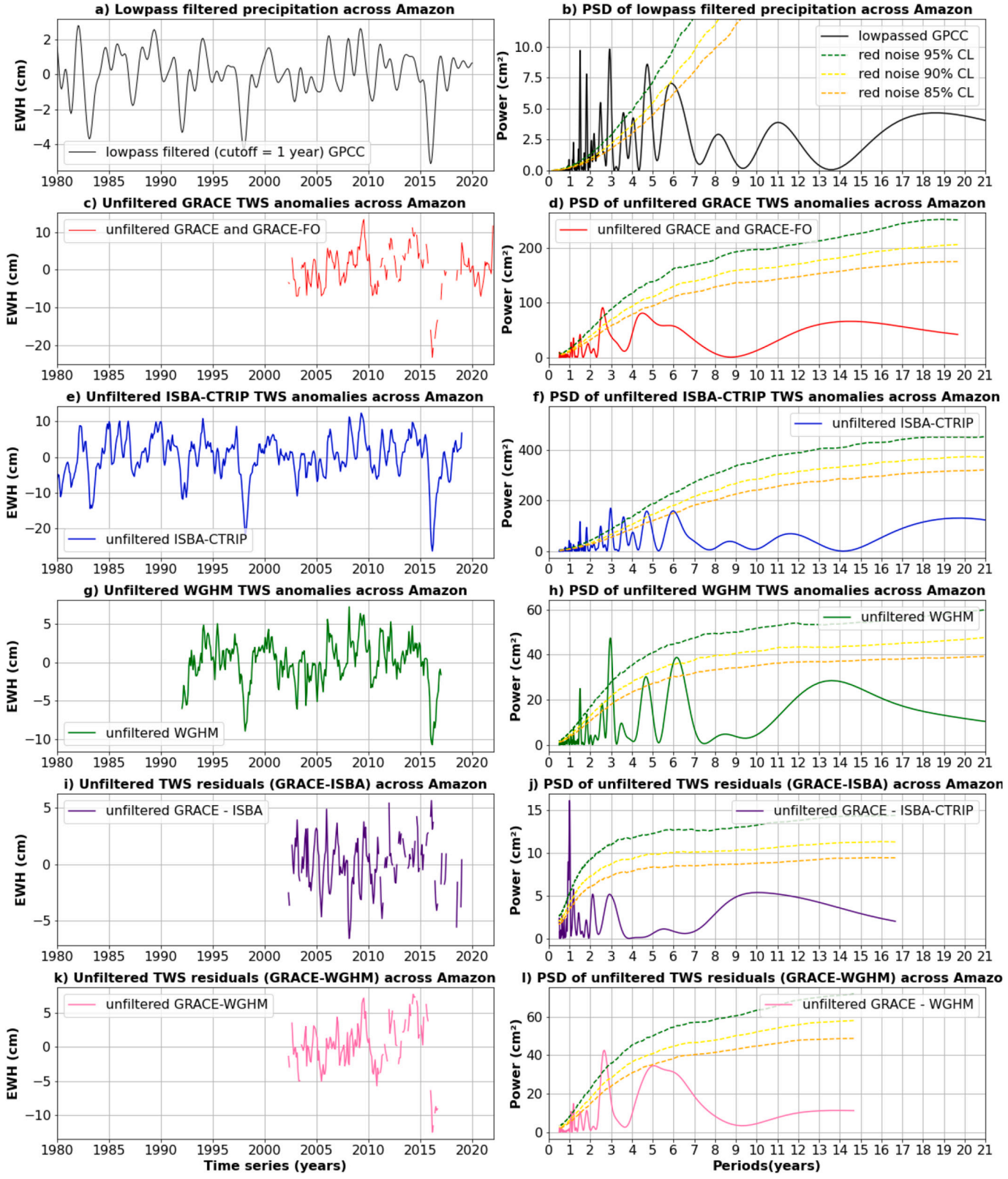

Fig. A4.2. Comparison of precipitation and TWS anomalies over the Amazon region (region R2 in Fig. 5). The layout is the same as for Fig. 6.

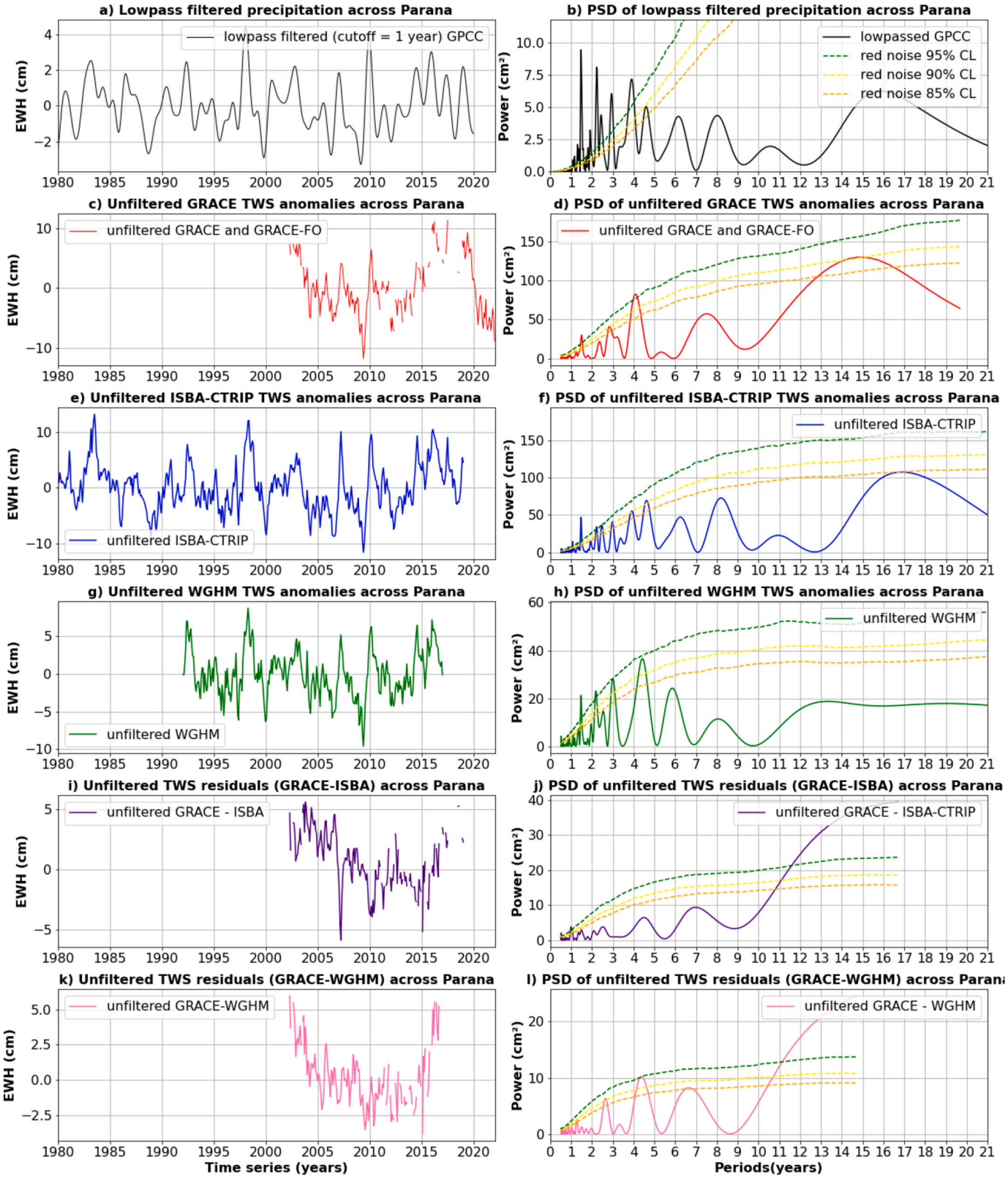

Fig. A4.3. Comparison of precipitation and TWS anomalies over the Parana region (region R3 in Fig. 5). The layout is the same as for Fig. 6.

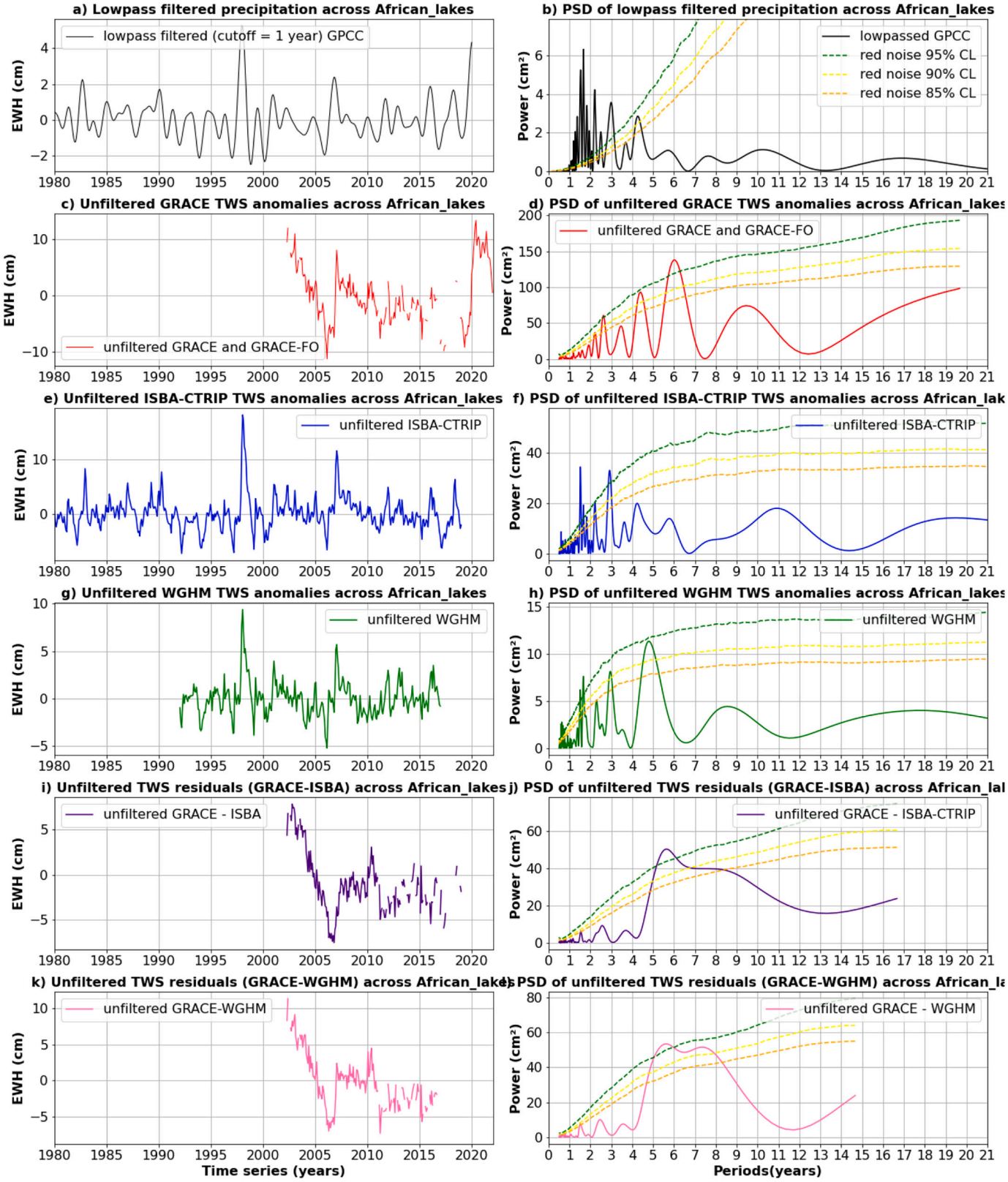

Fig. A4.4. Comparison of precipitation and TWS anomalies over the Great African Lakes region (region R5 in Fig. 5). The layout is the same as for Fig. 6.

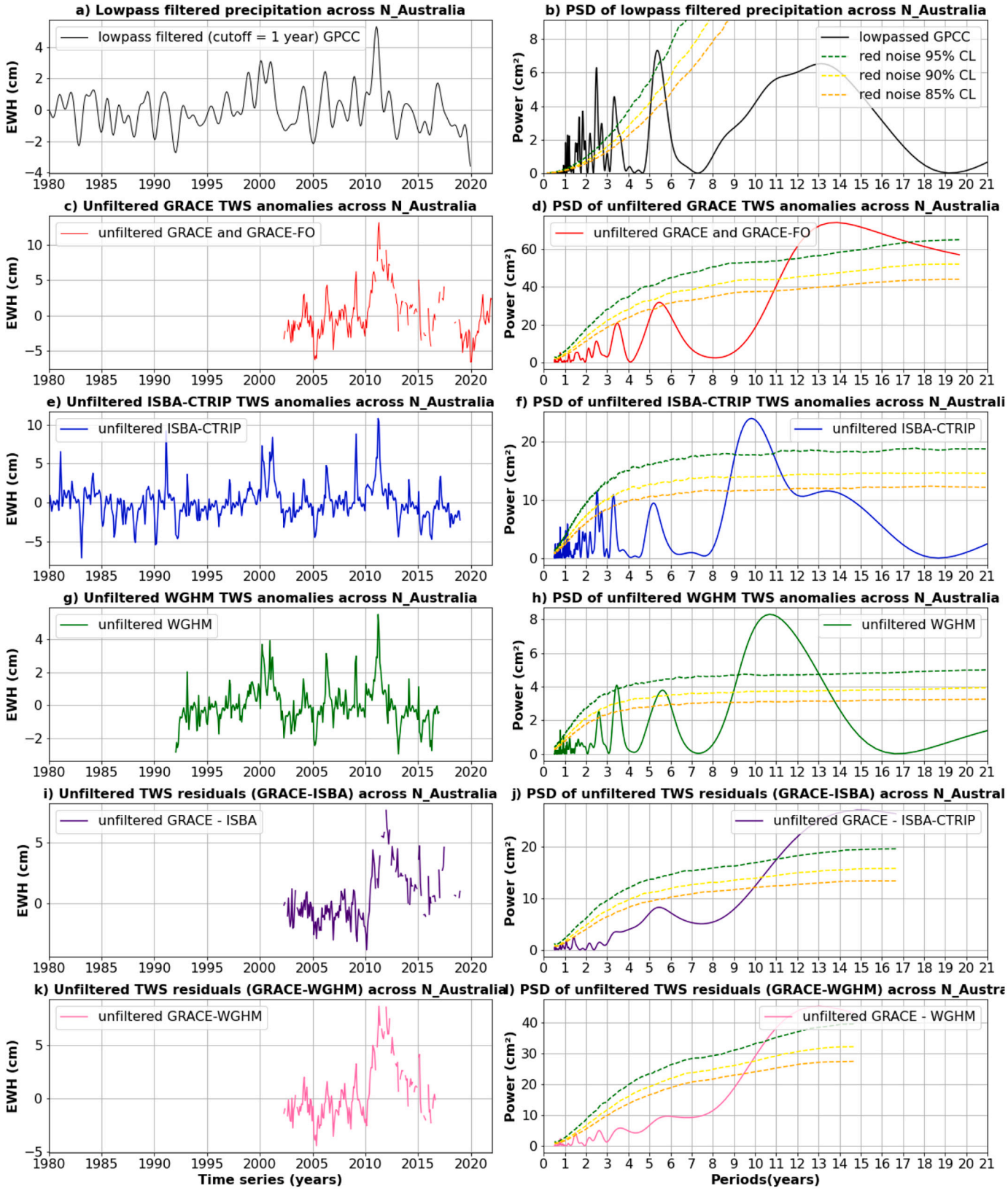

Fig. A4.5. Comparison of precipitation and TWS anomalies over North Australia (region R6 in Fig. 5). The layout is the same as for Fig. 6.

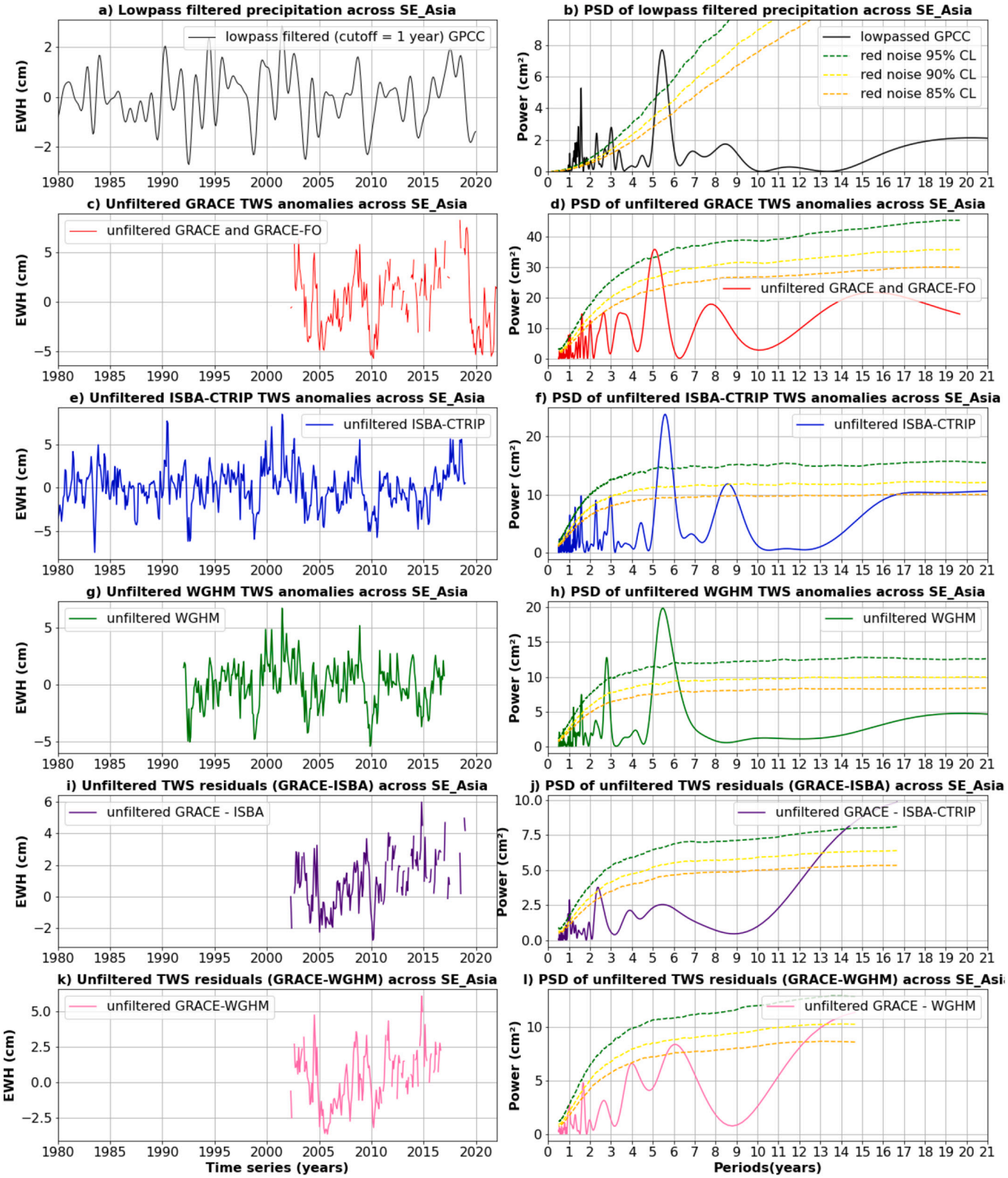

Fig. A4.6. Comparison of precipitation and TWS anomalies over South East Asia (region R7 in Fig. 5). The layout is the same as for Fig. 6.

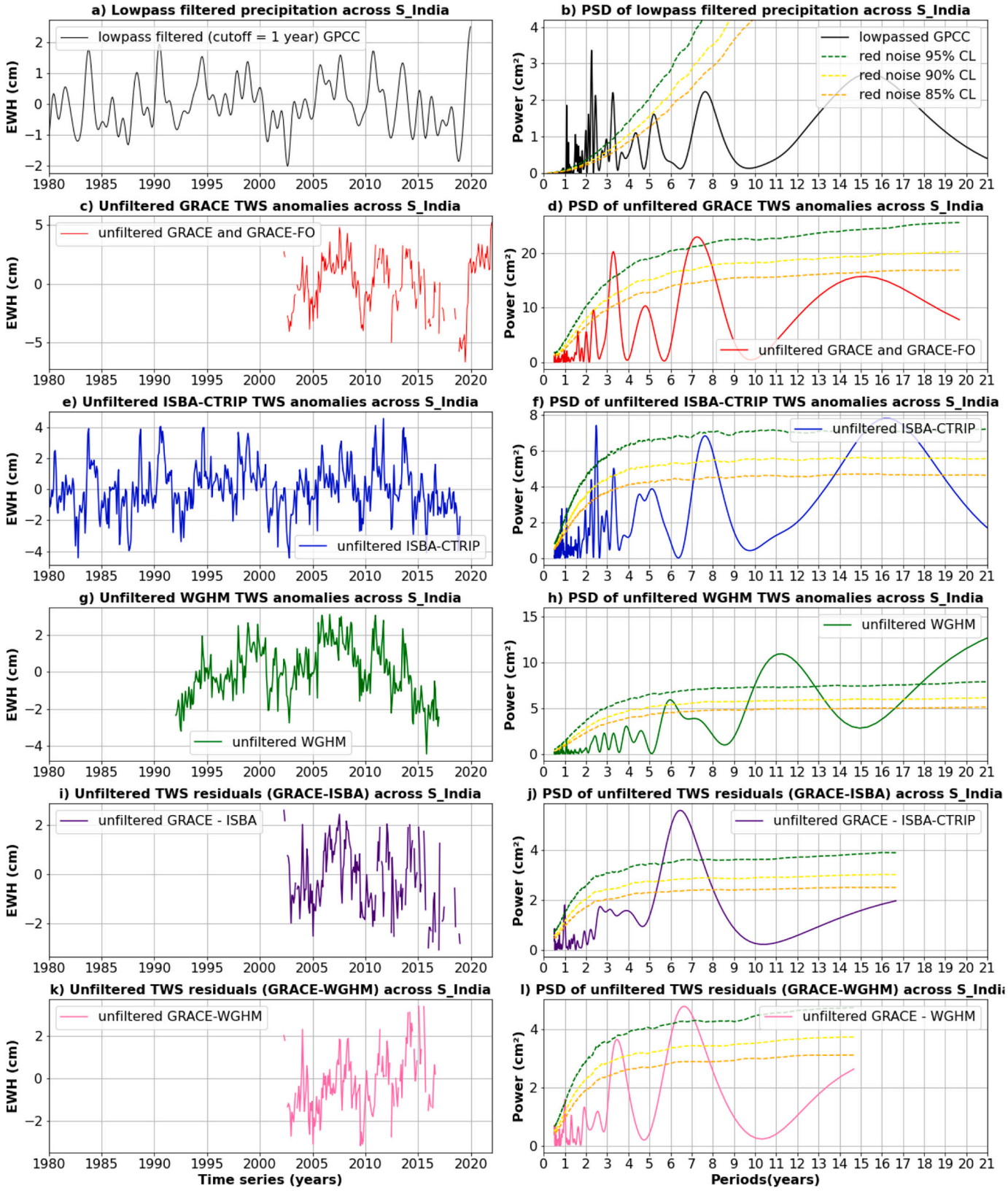

Fig. A4.7. Comparison of precipitation and TWS anomalies over the Indian Peninsula (region R8 in Fig. 5). The layout is the same as for Fig. 6.

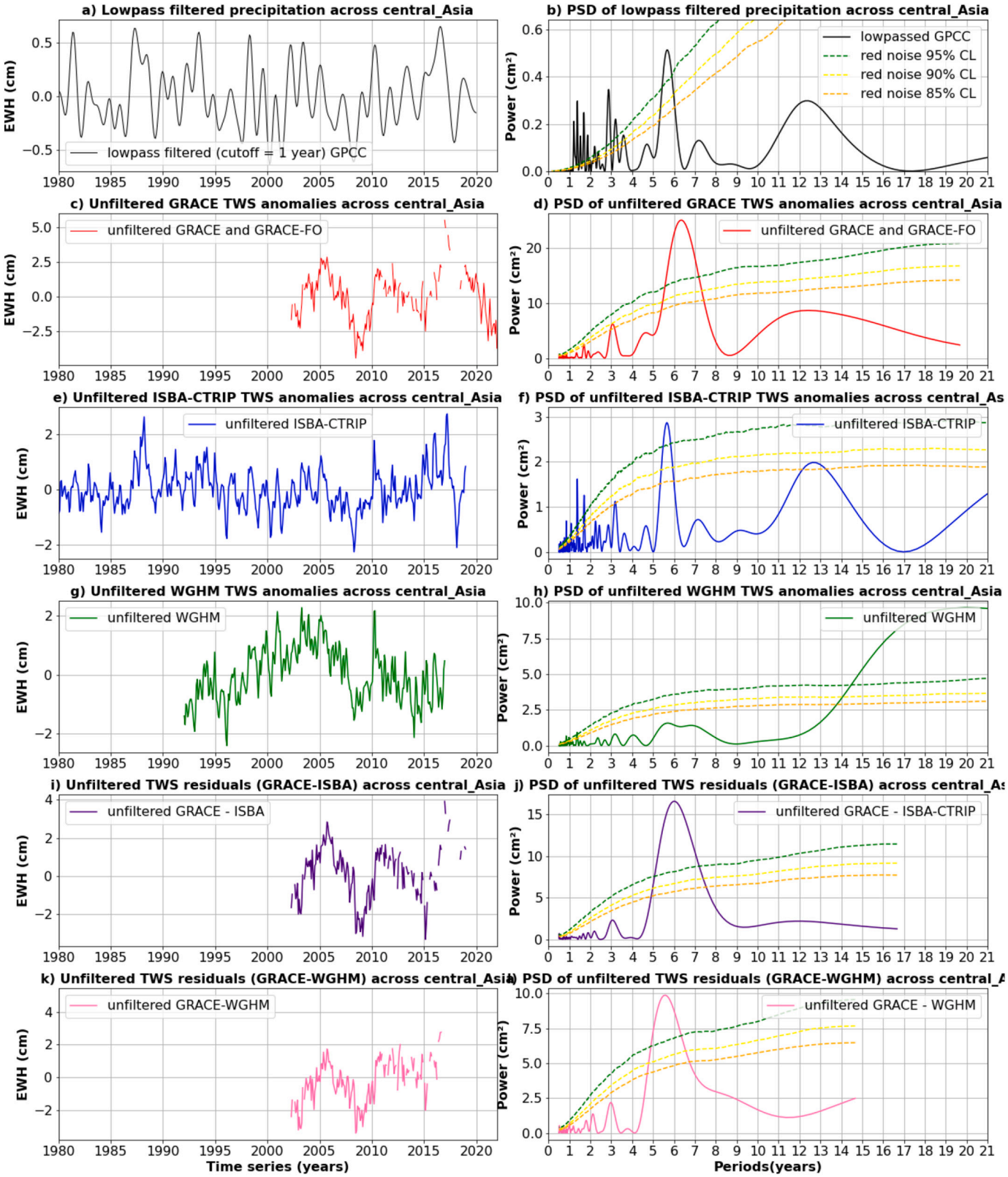

Fig. A4.8. Comparison of precipitation and TWS anomalies over central Asia (region R9 in Fig. 5). The layout is the same as for Fig. 6.

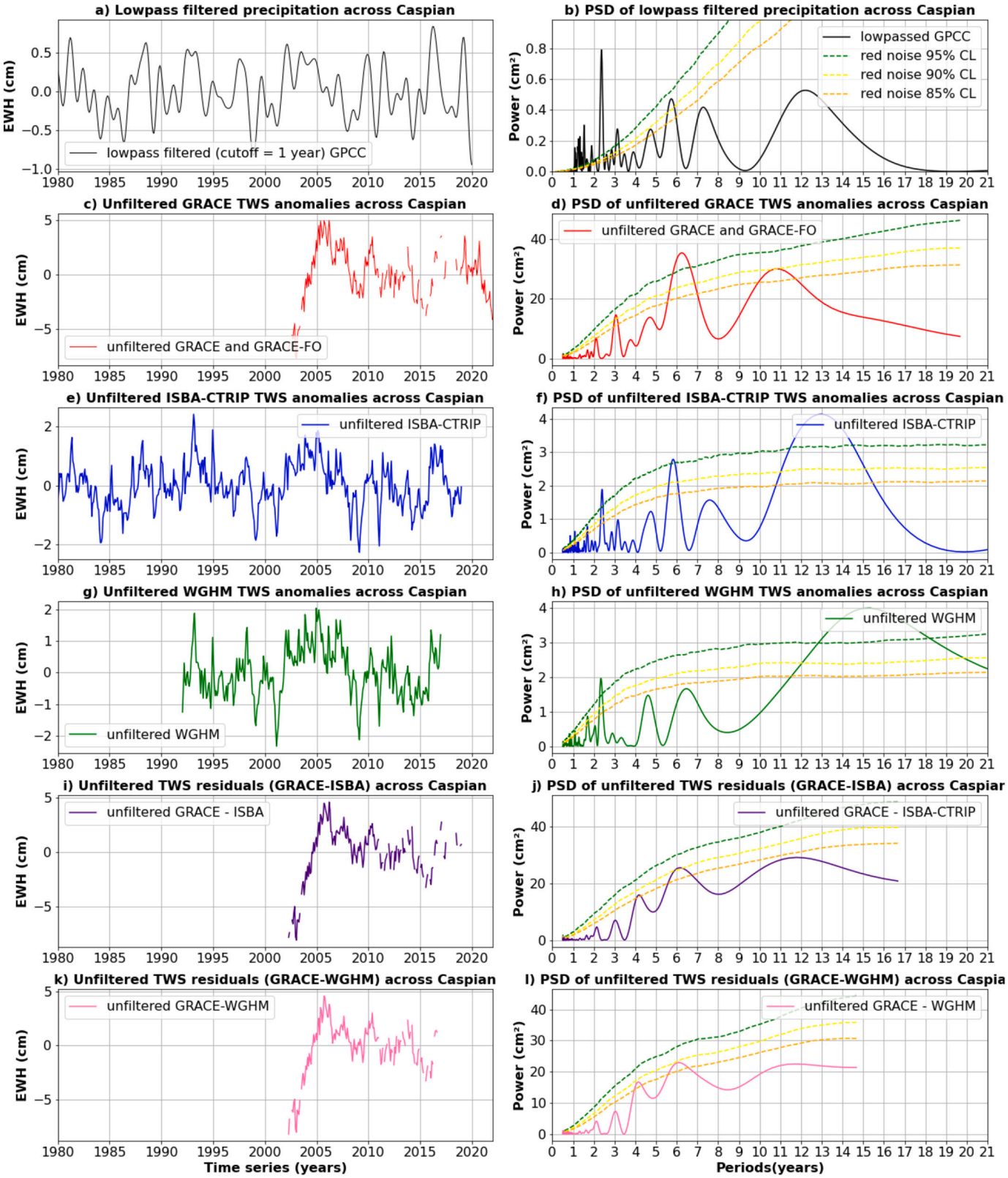

Fig. A4.9. Comparison of precipitation and TWS anomalies over the Caspian Sea region (region R10 in Fig. 5). The layout is the same as for Fig. 6.

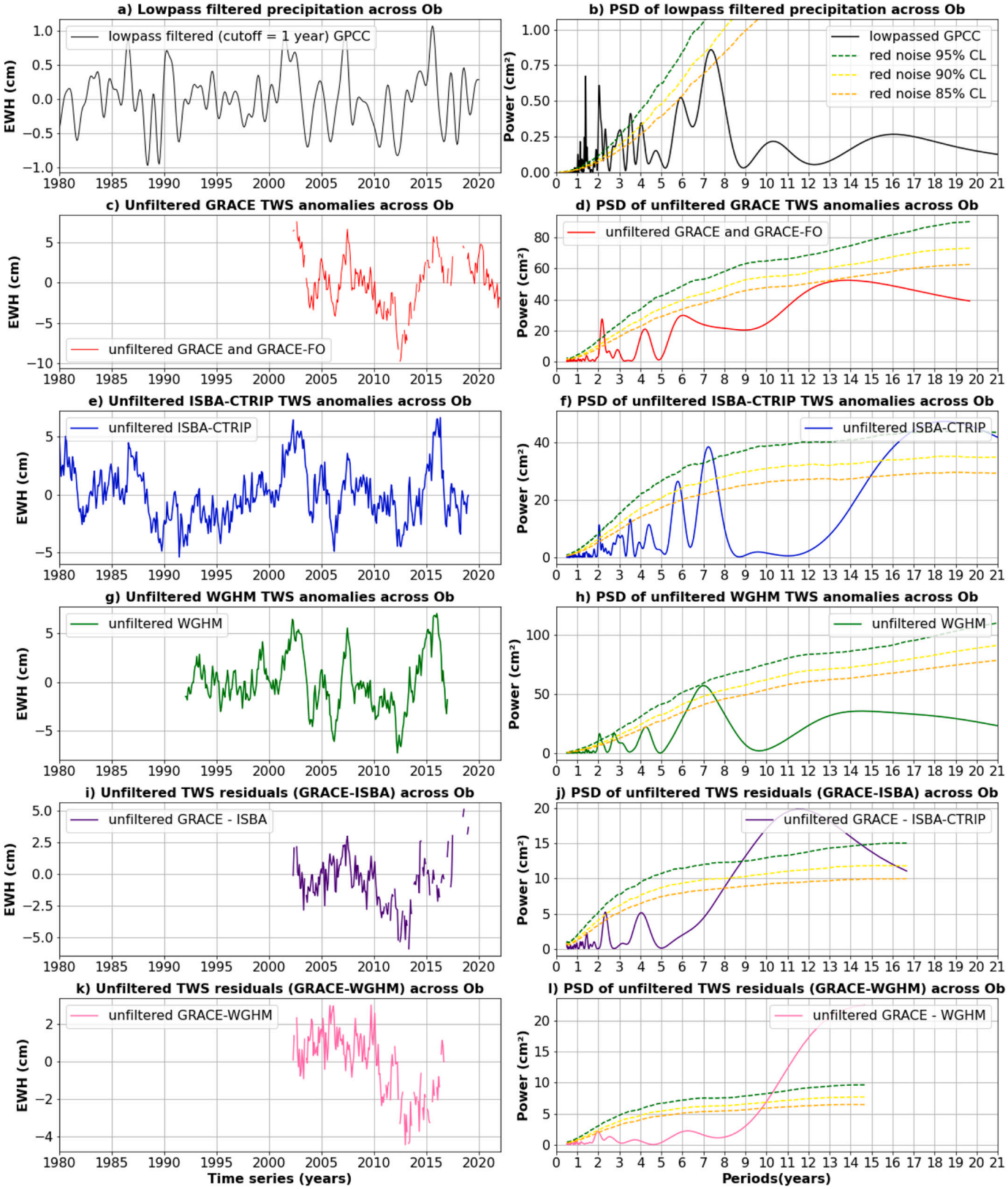

Fig. A4.10. Comparison of precipitation and TWS anomalies over the Ob region (region R11 in Fig. 5). The layout is the same as for Fig. 6.

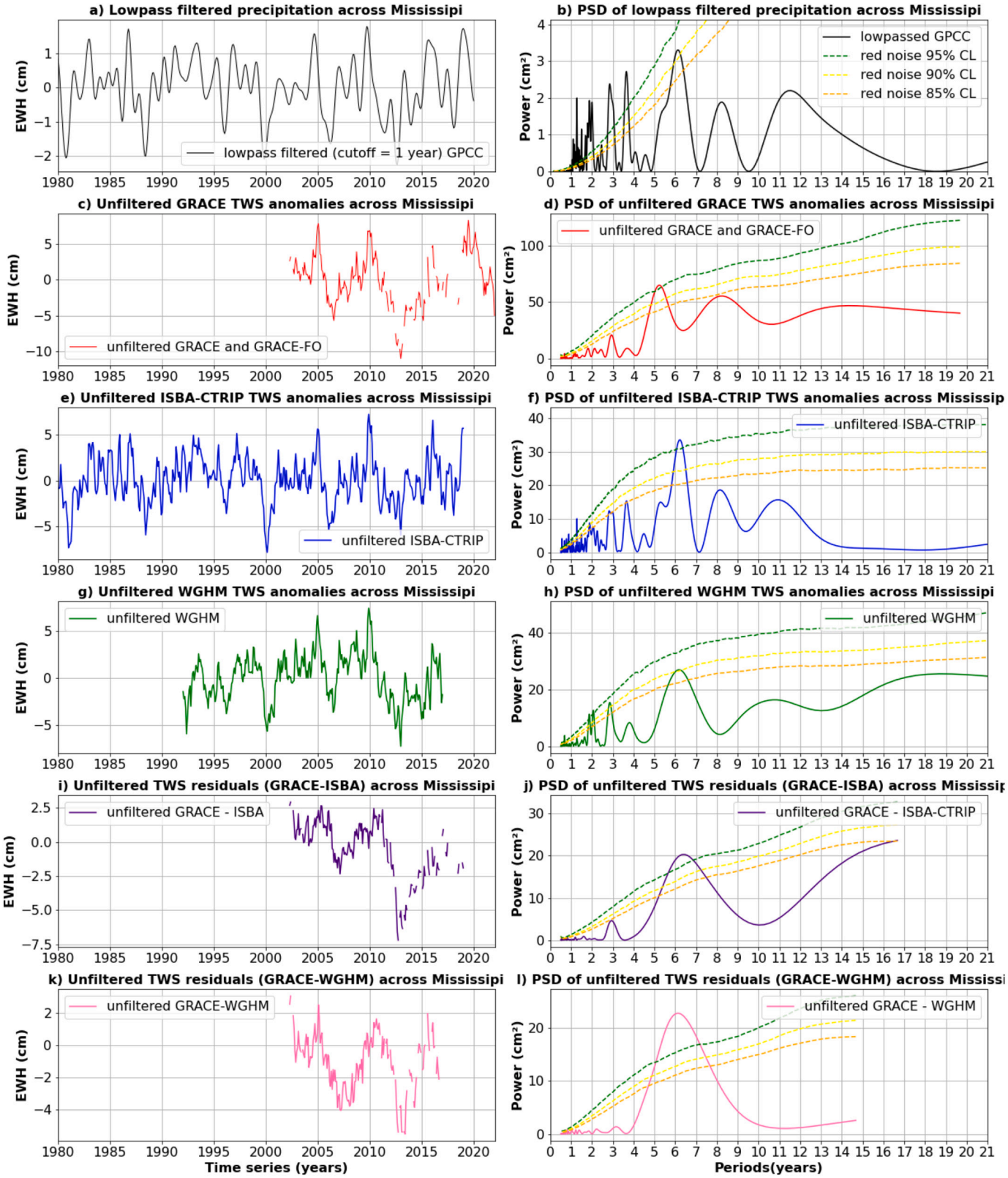

Fig. A4.11. Comparison of precipitation and TWS anomalies over the Mississippi region (region R12 in Fig. 5). The layout is the same as for Fig. 6.

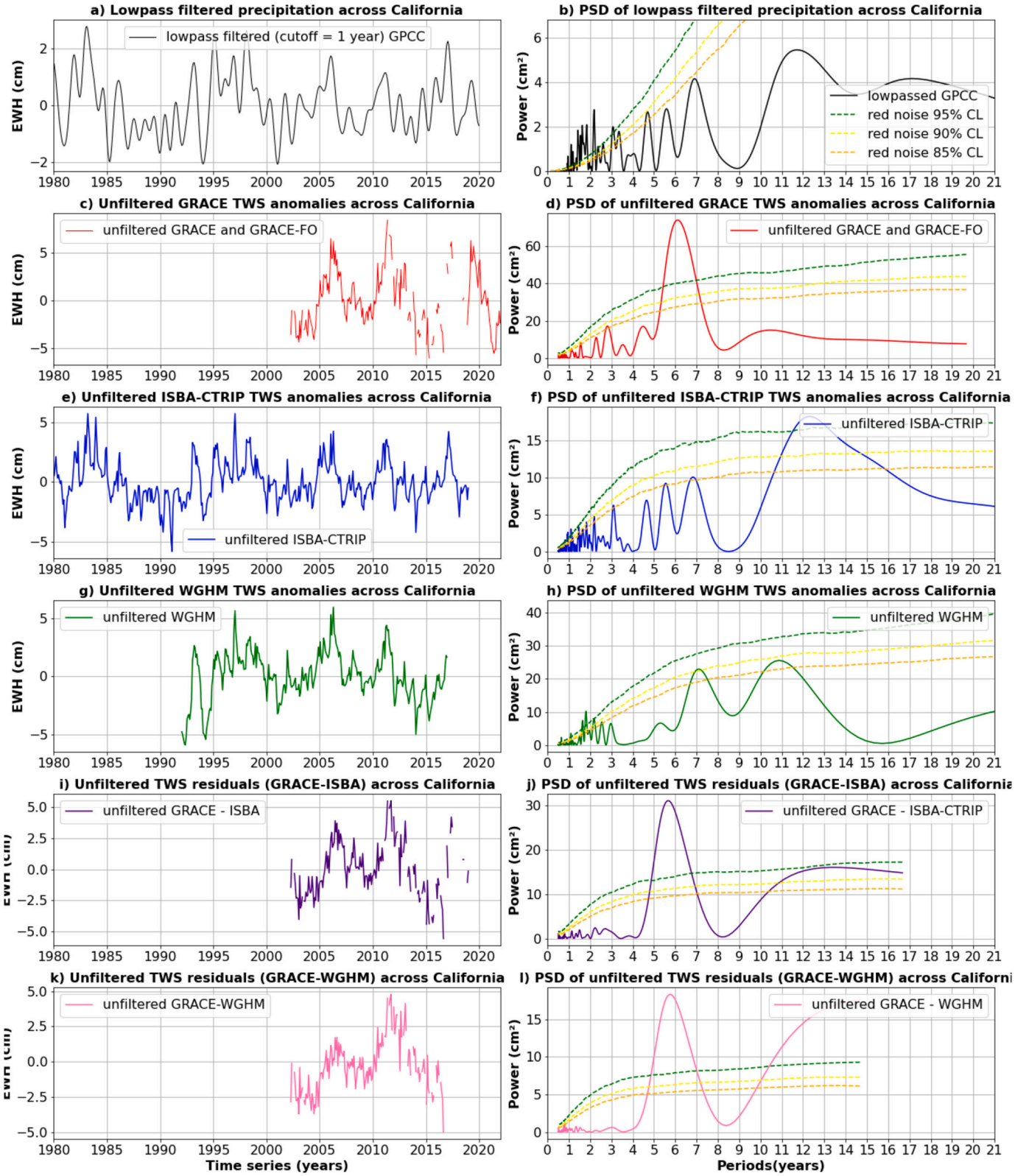

Fig. A4.12. Comparison of precipitation and TWS anomalies over the Central Valley region (region R13 in Fig. 5). The layout is the same as for Fig. 6.

References

Abarca del Rio, R., Gambis, D., Salstein, D.A., 2000. Interannual signals in length of day and atmospheric angular momentum. Ann. Geophys. 18, 347–364. https://doi.org/10.1007/s00585-000-0347-9.

Abarca del Rio, R., Gambis, D., Salstein, D., 2012. Interdecadal oscillations in Atmospheric Angular Momentum variations. J. Geodetic Sci. 2 (1), 42–52. https://doi.org/10.2478/v10156-011-0025-8.

Akvas, 2018. akvas/l3py: l3py v0.1.1 (v0.1.1), Zenodo. https://doi.org/10.5281/zenodo.1450900.

Aubert, J., 2018. Geomagnetic acceleration and rapid hydromagnetic wave dynamics in advanced numerical simulations of the geodynamo. Geophys. J. Int. 214 (1), 531–547.

Baerenzung, J., Holschneider, M., Wicht, J., et al., 2020. The Kalmag model as a candidate for IGRF-13. Earth Planets Space 72, 163. https://doi.org/10.1186/s40623-020-01295-y.

Barnes, R.T.H., Hide, R., White, A.A., Wilson, C.A., 1983. Atmospheric angular momentum fluctuations, length-of-day changes and polar motion. *Proceedings of the Royal Society of London.* A. Math. Phys. Sci. 387 (1792), 31–73.

Bizouard, C., Lambert, S., Gattano, C., et al., 2019. The IERS EOP 14C04 solution for Earth orientation parameters consistent with ITRF 2014. J. Geodyn. 93, 621–633. https://doi.org/10.1007/s00190-018-1186-3.

Buffett, B.A., 1996. A mechanism for decade fluctuations in the length of day. Geophys. Res. Lett. 23 (25), 3803–3806. https://doi.org/10.1029/96GL03571.

Buffett, B., 2014. Geomagnetic fluctuations reveal stable stratification at the top of the Earth's core. Nature 507 (7493), 484–487.

Buffett, B., Knezek, N., Holme, R., 2016. Evidence for MAC waves at the top of Earth's core and implications for variations in length of day. Geophys. J. Int. 204 (3), 1789–1800.

Cáceres, D., Marzeion, B., Malles, J.H., Gutknecht, B.D., Müller Schmied, H., Döll, P., 2020. Assessing global water mass transfers from continents to oceans over the period 1948–2016. Hydrol. Earth Syst. Sci. 24 (10), 4831–4851.

Chambers, D.P., Merrifield, M.A., Nerem, R.S., 2012. Is there a 60-year oscillation in global mean sea level? Geophys. Res. Lett. 39 (18).

Chao, B.F., 1989. Length-of-day variations caused by El Nino-Southern Oscillation and quasi-biennial oscillation. Science 243 (4893), 923–925. https://doi.org/10.1126/science.243.4893.923.

Chao, B.F., 2017. Dynamics of the inner core wobble under mantle-inner core gravitational interactions. J. Geophys. Res. Solid Earth 122 (9), 7437–7448. https://doi.org/10.1002/2017JB014405.

Chao, B.F., Yu, Y., 2020. Variation of the equatorial moments of inertia associated with a 6-year westward rotary motion in the Earth. Earth Planet. Sci. Lett. 542, 116316. https://doi.org/10.1016/j.epsl.2020.116316.

Chao, B.F., Zhou, Y.H., 1998. Meteorological excitation of interannual polar motion by the North Atlantic Oscillation. J. Geodyn. 27 (1), 61–73. https://doi.org/10.1016/S0264-3707(97)00030-6.

Chao, B.F., Chung, W., Shih, Z., Hsieh, Y., 2014. Earth's rotation variations: a wavelet analysis. Terra Nova 26 (4), 260–264. https://doi.org/10.1111/ter.12094.

Chen, J., 2005. Global mass balance and the length-of-day variation. J. Geophys. Res. 110, B08404 https://doi.org/10.1029/2004JB003474.

Chen, J.L., Wilson, C.R., Chao, B.F., Shum, C.K., Tapley, B.D., 2000. Hydrological and oceanic excitations to polar motion and length-of-day variation. Geophys. J. Int. 141 (1), 149–156. https://doi.org/10.1046/j.1365-246X.2000.00069.x.

Chen, J., Wilson, C.R., Kuang, W., Chao, B.F., 2019. Interannual oscillations in Earth rotation. J. Geophys. Res. Solid Earth 124, 13404–13414. https://doi.org/10.1029/2019JB018541.

Chen, J., Cazenave, A., Dahle, C., Llovel, W., Panet, I., Pfeffer, J., Moreira, L., 2022. Applications and challenges of GRACE and GRACE follow-on satellite gravimetry. Surv. Geophys. 1–41.

Cox, G.A., Livermore, P.W., Mound, J.E., 2016. The observational signature of modelled torsional waves and comparison to geomagnetic jerks. Phys. Earth Planet. Inter. 255, 50–65.

Currie, R.G., 1973. Geomagnetic line spectra-2 to 70 years. Astrophys. Space Sci. 21, 425–438.

Dahle, C., Flechtner, F., Murböck, M., Michalak, G., Neumayer, H., Abrykosov, O., Reinhold, A., König, R., 2018. GRACE Geopotential GSM Coefficients GFZ RL06, V. 6.0. GFZ Data Services. https://doi.org/10.5880/GFZ.GRACE_06_GSM.

De Viron, O., Dickey, J.O., 2014. The two types of El-Niño and their impacts on the length of day. Geophys. Res. Lett. 41, 3407–3412. https://doi.org/10.1002/2014GL059948.

De Viron, O., Marcus, S.L., Dickey, J.O., 2001. Atmospheric torques during the winter of 1989: Impact of ENSO and NAO positive phases. Geophys. Res. Lett. 28 (10), 1985–1988.

Decharme, B., Delire, C., Minvielle, M., Colin, J., Vergnes, J.-P., Alias, A., et al., 2019. Recent changes in the ISBA-CTRIP land surface system for use in the CNRM-CM6 climate model and in global off-line hydrological applications. J. Adv. Model. Earth Syst. 11, 1207–1252. https://doi.org/10.1029/2018MS001545.

Dickey, J., Marcus, S., Hide, R., 1992. Global propagation of interannual fluctuations in atmospheric angular momentum. Nature 357, 484–488. https://doi.org/10.1038/357484a0.

Ding, H., 2019. Attenuation and excitation of the ~6-year oscillation in the length-of-day variation. Earth Planet. Sci. Lett. 507, 131–139. https://doi.org/10.1016/j.epsl.2018.12.003.

Ding, H., Chao, B.F., 2018. A 6-year westward rotary motion in the Earth: Detection and possible MICG coupling mechanism. Earth Planet. Sci. Lett. 495, 50–55. https://doi.org/10.1016/j.epsl.2018.05.009.

Ding, H., An, Y., Shen, W., 2021a. New evidence for the fluctuation characteristics of intradecadal periodic signals in length-of-day variation. J. Geophys. Res. Solid Earth *126* (2). https://doi.org/10.1029/2020JB020990 e2020JB020990.

Ding, H., Jin, T., Li, J., Jiang, W., 2021b. The contribution of a newly unraveled 64 years common oscillation on the estimate of present-day global mean sea level rise. J. Geophys. Res. Solid Earth *126* (8) e2021JB022147.

Ditmar, P., 2018. Conversion of time-varying Stokes coefficients into mass anomalies at the Earth's surface considering the Earth's oblateness. J. Geod. 92 (12), 1401–1412.

Dobrica, V., Demetrescu, C., Mandea, M., 2018. Geomagnetic field declination: from decadal to centennial scales. Solid Earth 9 (2), 491–503.

Dobslaw, H., Bergmann-Wolf, I., Dill, R., Poropat, L., Thomas, M., Dahle, C., Flechtner, F., 2017. A new high-resolution model of non-tidal atmosphere and ocean mass variability for de-aliasing of satellite gravity observations: AOD1B RL06. Geophys. J. Int. 211 (1), 263–269.

Duan, P., Huang, C., 2020. Intradecadal variations in length of day and their correspondence with geomagnetic jerks. Nat. Commun. 11, 2273. https://doi.org/10.1038/s41467-020-16109-8.

Duan, P., Liu, G., Liu, L., Hu, X., Hao, X., Huang, Y., Wang, B., 2015. Recovery of the 6-year signal in length of day and its long-term decreasing trend. Earth Planet Sp 67, 161. https://doi.org/10.1186/s40623-015-0328-6.

Dumberry, M., 2010. Gravity variations induced by core flows. Geophys. J. Int. 180 (2), 635–650. https://doi.org/10.1111/j.1365-246X.2009.04437.x.

Dumberry, M., Mandea, M., 2022. Gravity variations and ground deformations resulting from core dynamics. Surv. Geophys. 43 (1), 5–39. https://doi.org/10.1007/s10712-021-09656-2.

Egger, J., Weickmann, K., Hoinka, K.-P., 2007. Angular momentum in the global atmospheric circulation. Rev. Geophys. 45, RG4007 https://doi.org/10.1029/2006RG000213.

Enfield, D.B., Mestas-Nuñez, A.M., Trimble, P.J., 2001. The Atlantic multidecadal oscillation and its relation to rainfall and river flows in the continental U.S. Geophys. Res. Lett. 28, 2077–2080. https://doi.org/10.1029/2000GL012745.

Eubanks, T.M., Steppe, J.A., Dickey, J.O., Callahan, P.S., 1985. A spectral analysis of the Earth's angular momentum budget. J. Geophys. Res. 90 (B7), 5385–5404. https://doi.org/10.1029/JB090iB07p05385.

Finlay, C.C., Kloss, C., Olsen, N., et al., 2020. The CHAOS-7 geomagnetic field model and observed changes in the South Atlantic Anomaly. Earth Planets Space 72, 156. https://doi.org/10.1186/s40623-020-01252-9.

Foreman, M.G.G., Henry, R.F., 1989. The harmonic analysis of tidal model time series. Adv. Water Resour. 12, 109–120.

Gerick, F., Jault, D., Noir, J., 2021. Fast quasi-geostrophic Magneto-Coriolis modes in the Earth's core. Geophys. Res. Lett. 48 https://doi.org/10.1029/2020GL090803 e2020GL090803.

Ghil, M., Allen, M.R., Dettinger, M.D., Ide, K., Kondrashov, D., Mann, M.E., Robertson, A. W., Saunders, A., Tian, Y., Varadi, F., Yiou, P., 2002. Advanced spectral methods for climatic time series. Rev. Geophys. 40 (1), 1003. https://doi.org/10.1029/2000RG000092.

Gillet, N., Pais, M.A., Jault, D., 2009. Ensemble inversion of time-dependent core flow models. Geochem. Geophys. Geosyst. 10, Q06004 https://doi.org/10.1029/2008GC002290.

Gillet, N., Jault, D., Canet, E., et al., 2010. Fast torsional waves and strong magnetic field within the Earth's core. Nature 465, 74–77. https://doi.org/10.1038/nature09010.

Gillet, N., Jault, D., Finlay, C.C., 2015. Planetary gyre, time-dependent eddies, torsional waves, and equatorial jets at the Earth's core surface. J. Geophys. Res. Solid Earth 120, 3991–4013. https://doi.org/10.1002/2014JB011786.

Gillet, N., Dumberry, M., Rosat, S., 2021. The limited contribution from outer core dynamics to global deformations at the Earth's surface. Geophys. J. Int. 224 (1), 216–229. https://doi.org/10.1093/gji/ggaa448.

Gillet, N., Gerick, F., Jault, D., Schwaiger, T., Aubert, J., Istas, M., 2022a. Satellite magnetic data reveal interannual waves in Earth's core. Proc. Natl. Acad. Sci. 119 (13), e2115258119 https://doi.org/10.1073/pnas.2115258119.

Gillet, N., Gerick, F., Angappan, R., et al., 2022b. A dynamical prospective on interannual geomagnetic field changes. Surv. Geophys. 43, 71–105. https://doi.org/10.1007/s10712-021-09664-2.

Godin, G., 1972. The Analysis of Tides. University of Toronto Press, 264 pp.

Gorshkov, V.L., 2010. Study of the interannual variations of the Earth's rotation. Sol. Syst. Res. 44, 487–497. https://doi.org/10.1134/S003809461006002X.

Goux, O., Pfeffer, J., Blazquez, A., Weaver, A.T., Ablain, M., 2023. A mass conserving filter based on diffusion for Gravity Recovery and Climate Experiment (GRACE) spherical harmonics solutions. Geophys. J. Int. https://doi.org/10.1093/gji/ggad016 ggad016.

GRACE-FO, 2022a. GRACEFO_L2_JPL_MONTHLY_0061. Ver. 6.1. PO.DAAC, CA, USA. https://doi.org/10.5067/GFL20-MJ061.

GRACE-FO, 2022b. GRACEFO_L2_CSR_MONTHLY_0061. Ver. 6.1. PO.DAAC, CA, USA. Dataset accessed 023-01-05 at https://doi.org/10.5067/GFL20-MC061.

Gross, R.S., Marcus, S.L., Eubanks, T.M., Dickey, J.O., Keppenne, C.L., 1996. Detection of an ENSO signal in seasonal length-of-day variations. Geophys. Res. Lett. 23 (23), 3373–3376. https://doi.org/10.1029/96GL03260.

Hide, R., Clayton, R.W., Hager, B.H., Spieth, M.A., Voorhdes, C.V., 1993. Topographic core-mantle coupling and fluctuations in the Earth's rotation. In: Relating Geophysical Structures and Processes: The Jeffreys Volume. Geophys. Monogr. Ser., vol. 76, edited by K. Aki and R. Dmowska. AGU, Washington, D. C, pp. 107–120. https://doi.org/10.1029/GM076p0107.

Holme, R., de Viron, O., 2013. Characterization and implications of intradecadal variations in length of day. Nature 499 (7457), 202–204. https://doi.org/10.1038/nature12282.

Hsu, C.C., Duan, P.S., Xu, X.Q., Zhou, Y.H., Huang, C.L., 2021. On the~ 7 year periodic signal in length of day from a frequency domain stepwise regression method. J. Geod. 95 (5), 55. https://doi.org/10.1007/s00190-021-01503-x.

Huder, L., Gillet, N., Finlay, C.C., et al., 2020. COV-OBS.x2: 180 years of geomagnetic field evolution from ground-based and satellite observations. Earth Planets Space **72**, 160. https://doi.org/10.1186/s40623-020-01194-2.

Huffman, G.J., Stocker, E.F., Bolvin, D.T., Nelkin, E.J., Tan, J., 2019. GPM IMERG Final Precipitation L3 1 month 0.1 degree x 0.1 degree V06, Greenbelt, MD, Goddard Earth Sciences Data and Information Services Center (GES DISC). Accessed: 26 January 2022. https://doi.org/10.5067/GPM/IMERG/3B-MONTH/06.

Istas, M., Gillet, N., Finlay, C.C., Hammer, M.D., Huder, L., 2023. Transient core surface dynamics from ground and satellite geomagnetic data. Geophys. J. Int. 233 (3), 1890–1915. https://doi.org/10.1093/gji/ggad039.

Jackson, L.P., Mound, J.E., 2010. Geomagnetic variation on decadal time scales: what can we learn from empirical mode decomposition? Geophys. Res. Lett. 37 (14).

Jajcay, N., Hlinka, J., Kravtsov, S., Tsonis, A.A., Paluš, M., 2016. Time scales of the European surface air temperature variability: the role of the 7-8 year cycle. Geophys. Res. Lett. 43 (2), 902–909. https://doi.org/10.1002/2015GL067325.

Jault, D., Gire, C., Le Mouel, J.L., 1988. Westward drift, core motions and exchanges of angular momentum between core and mantle. Nature 333 (6171), 353–356. https://doi.org/10.1038/333353a0.

Lambeck, K., 1980. The Earth's Variable Rotation: Geophysical Causes and Consequences, 449 pages. Cambridge University Press.

Lecomte, H., Rosat, S., Mandea, M., Boy, J.P., Pfeffer, J., 2023. Uncertainty of low-degree space gravimetry observations: Surface processes versus Earth's core signal. J. Geophys. Res. Solid Earth 128, e2023JB026503. https://doi.org/10.1029/2023JB026503.

Lemoine, J.M., Bourgogne, S., 2020. RL05 monthly and 10-day gravity field solutions from CNES/GRGS (No. GSTM2020–51), Copernicus Meetings.

Lesur, V., Gillet, N., Hammer, M.D., et al., 2022. Rapid variations of Earth's core magnetic field. Surv. Geophys. 43, 41–69. https://doi.org/10.1007/s10712-021-09662-4.

Loomis, B.D., Luthcke, S.B., Sabaka, T.J., 2019a. Regularization and error characterization of GRACE mascons. J. Geodyn. 93, 1381–1398. https://doi.org/10.1007/s00190-019-01252-y.

Loomis, B.D., Rachlin, K.E., Luthcke, S.B., 2019b. Improved Earth oblateness rate reveals increased ice sheet losses and mass-driven sea level rise. Geophys. Res. Lett. 46 (12), 6910–6917.

Mandea, M., Panet, I., Lesur, V., De Viron, O., Diament, M., Le Mouël, J.L., 2012. Recent changes of the Earth's core derived from satellite observations of magnetic and gravity fields. Proc. Natl. Acad. Sci. 109 (47), 19129–19133. https://doi.org/10.1073/pnas.1207346109.

Mandea, M., Narteau, C., Panet, I., Le Mouël, J.L., 2015. Gravimetric and magnetic anomalies produced by dissolution-crystallization at the core-mantle boundary. J. Geophys. Res. Solid Earth 120 (9), 5983–6000. https://doi.org/10.1002/2015JB012048.

Mandea, M., Dehant, V., Cazenave, A., 2020. GRACE—gravity data for understanding the deep Earth's interior. Remote Sens. 12, 4186. https://doi.org/10.3390/rs12244186.

Marcus, S.L., 2016. Does an intrinsic source generate a shared low-frequency signature in Earth's climate and rotation rate? Earth Interact. 20 (4), 1–14. https://doi.org/10.1175/EI-D-15-0014.1.

Mayer-Gürr, T., Behzadpour, S., Ellmer, M., Kvas, A., Klinger, B., Strasser, S., Zehentner, N., 2018. ITSG-Grace2018 - Monthly, Daily and Static Gravity Field Solutions from GRACE. GFZ Data Services. https://doi.org/10.5880/ICGEM.2018.003.

Meyer, P.G., Kantz, H., 2019. A simple decomposition of European temperature variability capturing the variance from days to a decade. Clim. Dyn. 53 (11), 6909–6917. https://doi.org/10.1007/s00382-019-04965-0.

Meyer, U., Lasser, M., Jaeggi, A., Dahle, C., Flechtner, F., Kvas, A., Behzadpour, S., Mayer-Gürr, T., Lemoine, J., Koch, I., Flury, J., Bourgogne, S., 2020. International Combination Service for Time-Variable Gravity Fields (COST-G) Monthly GRACE-FO Series, V. 01. GFZ Data Services. https://doi.org/10.5880/ICGEM.COST-G.002.

Moreira, L., Cazenave, A., Palanisamy, H., 2021. Influence of interannual variability in estimating the rate and acceleration of present-day global mean sea level. Glob. Planet. Chang. 199, 103450. https://doi.org/10.1016/j.gloplacha.2021.103450.

Morice, C.P., Kennedy, J.J., Rayner, N.A., Winn, J.P., Hogan, E., Killick, R.E., et al., 2021. An updated assessment of near-surface temperature change from 1850: the HadCRUT5 data set. J. Geophys. Res.-Atmos. 126 https://doi.org/10.1029/2019JD032361 e2019JD032361.

Mound, J.E., Buffett, B.A., 2003. Interannual oscillations in length of day: Implications for the structure of the mantle and core. J. Geophys. Res. 108 (B7), 2334. https://doi.org/10.1029/2002JB002054.

Mound, J.E., Buffett, B.A., 2006. Detection of a gravitational oscillation in length-of-day. Earth Planet. Sci. Lett. 243 (3–4), 383–389. https://doi.org/10.1016/j.epsl.2006.01.043.

Müller Schmied, H., Cáceres, D., Eisner, S., Flörke, M., Herbert, C., Niemann, C., Peiris, T. A., Popat, E., Portmann, F.T., Reinecke, R., Schumacher, M., Shadkam, S., Telteu, C.-E., Trautmann, T., Döll, P., 2021. The global water resources and use model WaterGAP v2.2d: model description and evaluation. Geosci. Model Dev. 14, 1037–1079. https://doi.org/10.5194/gmd-14-1037-2021.

Munk, W.H., MacDonald, G.J.F., 1960. The Rotation of the Earth. Cambridge University Press, London, 323 pages.

North, G.R., 1984. Empirical orthogonal functions and normal modes. J. Atmos. Sci. 41 (5), 879–887. https://doi.org/10.1175/1520-0469(1984)041<0879:EOFANM>2.0.CO;2.

Pais, M.A., Jault, D., 2008. Quasi-geostrophic flows responsible for the secular variation of the Earth's magnetic field. Geophys. J. Int. 173 (2), 421–443.

Peltier, W.R., Argus, D.F., Drummond, R., 2018. Comment on the paper by Purcell et al. 2016 entitled An assessment of ICE-6G_C (VM5a) glacial isostatic adjustment model. J. Geophys. Res. Solid Earth 122.

Pfeffer, J., Cazenave, A., Blazquez, A., Decharme, B., Munier, S., Barnoud, A., 2023. Assessment of pluriannual and decadal changes in terrestrial water storage predicted by global hydrological models in comparison with GRACE satellite gravity mission. Accepted for publication in Hydrology and Earth System Sciences on September 6, 2023. EGUsphere [preprint]. https://doi.org/10.5194/egusphere-2022-1032.

Rekier, J., Chao, B.F., Chen, J., et al., 2022. Earth's Rotation: Observations and Relation to Deep Interior. Surv. Geophys. 43, 149–175. https://doi.org/10.1007/s10712-021-09669-x.

Roberts, P.H., Yu, Z.J., Russell, C.T., 2007. On the 60-year signal from the core. Geophys. Astrophys. Fluid Dynam. 101 (1), 11–35.

Rosat, S., Gillet, N., 2023. Intradecadal variations in length of day: coherence with models of the Earth's core dynamics. Phys. Earth Planet. Inter. 341, 107053 https://doi.org/10.1016/j.pepi.2023.107053.

Rosat, S., Gillet, N., Boy, J.P., Couhert, A., Dumberry, M., 2021. Interannual variations of degree 2 from geodetic observations and surface processes. Geophys. J. Int. 225 (1), 200–221. https://doi.org/10.1093/gji/ggaa590.

Rosen, R.D., Salstein, D.A., Eubanks, T.M., Dickey, J.O., Steppe, J.A., 1984. An El Niño Signal in Atmospheric Angular Momentum and Earth Rotation. Science 225, 411–414. https://doi.org/10.1126/science.225.4660.411.

Salstein, D.A., Kann, D.M., Miller, A.J., Rosen, R.D., 1993. The sub-bureau for atmospheric angular momentum of the international earth rotation service: a meteorological data center with geodetic applications. Bull. Amer. Meteor. Soc. 74, 67–80.

Salstein, D.A., Rosen, R.D., 1997. Global momentum and energy signals from reanalysis systems. Preprints, 7th Conf. on Climate Variations, American Meteorological Society, Boston, MA, pp. 344–348.

Salstein, D.A., Zhou, Y.H., Chen, J.L., 2005. Revised Angular Momentum Datasets for Atmospheric Angular Momentum Studies, European Geophysical Union (EGU) Spring Meetingv.

Saraswati, A.T., de Viron, O., Mandea, M., 2023. Earth's core variability from the magnetic and gravity field observations. EGUsphere [preprint]. https://doi.org/10.5194/egusphere-2023-856. submitted to Solid Earth.

Save, H., 2020. CSR GRACE and GRACE-FO RL06 Mascon Solutions v02. https://doi.org/10.15781/cgq9-nh24.

Save, H., Bettadpur, S., Tapley, B.D., 2016. High resolution CSR GRACE RL05 mascons. J. Geophys. Res. Solid Earth 121. https://doi.org/10.1002/2016JB013007.

Schlesinger, M.E., Ramankutty, N., 1994. An oscillation in the global climate system of period 65–70 years. Nature 367 (6465), 723–726.

Schneider, U., Becker, A., Finger, P., et al., 2014. GPCC's new land surface precipitation climatology based on quality-controlled in situ data and its role in quantifying the global water cycle. Theor. Appl. Climatol. 115, 15–40. https://doi.org/10.1007/s00704-013-0860-x.

Schulz, M., Mudelsee, M., 2002. REDFIT: estimating red-noise spectra directly from unevenly spaced paleoclimatic time series. Comput. Geosci. 28 (3), 421–426. https://doi.org/10.1016/S0098-3004(01)00044-9!!.

Silva, L., Jackson, L., Mound, J., 2012. Assessing the importance and expression of the 6-year geomagnetic oscillation. J. Geophys. Res. 117, B10101 https://doi.org/10.1029/2012JB009405.

Sun, Y., Riva, R., Ditmar, P., 2016. Optimizing estimates of annual variations and trends in geocenter motion and J2 from a combination of GRACE data and geophysical models. J. Geophys. Res. Solid Earth 121 (11), 8352–8370.

Tang, L., Li, J., Chen, J., Wang, S.Y., Wang, R., Hu, 2020. Seismic impact of large earthquakes on estimating global mean ocean mass change from GRACE. Remote Sens. 12 (6), 935.

VanderPlas, J.T., 2018. Understanding the lomb–scargle periodogram. Astrophys. J. Suppl. Ser. 236 (1), 16. https://doi.org/10.3847/1538-4365/aab766.

Vondrák, J., Burša, M., 1977. The rotation of the Earth between 1955.5 and 1976.5. Stud. Geophys. Geod. 21, 107–117. https://doi.org/10.1007/BF01634821.

Watkins, A., Fu, Y., Gross, R., 2018. Earth's subdecadal angular momentum balance from deformation and rotation data. Sci. Rep. 8, 13761. https://doi.org/10.1038/s41598-018-32043-8.

Weickmann, K.M., Sardeshmukh, P.D., 1994. The atmospheric angular momentum cycle associated with a Madden–Julian oscillation. J. Atmos. Sci. 51 (21), 3194–3208.

Wiese, D.N., Yuan, D.-N., Boening, C., Landerer, F.W., Watkins, M.M., 2019. JPL GRACE and GRACE-FO Mascon Ocean, Ice, and Hydrology Equivalent Water Height JPL RL06 Version 02. Ver. 2. PO.DAAC, CA, USA, Dataset accessed 2022-01-05 at. https://doi.org/10.5067/TEMSC-3MJ62.

Yang, Y., Song, X., 2023. Multidecadal variation of the Earth's inner-core rotation. Nat. Geosci. 16, 182–187. https://doi.org/10.1038/s41561-022-01112-z.

Yuan, D.-N., 2019. GRACE Follow-On Level-2 Gravity Field Product User Handbook, JPL D-103922. https://podaac-tools.jpl.nasa.gov/drive/files/allData/gracefo/docs/GRACE-FO_L2-UserHandbook_v1.0.pdf.

Zhou, Y.H., Salstein, D.A., Chen, J.L., 2006. Revised atmospheric excitation function series related to Earth variable rotation under consideration of surface topography. J. Geophys. Res. 111, D12108 https://doi.org/10.1029/2005JD006608.

Zotov, L., Bizouard, C., Shum, C.K., 2016. A possible interrelation between Earth rotation and climatic variability at decadal time-scale. Geodesy Geodynam. 7 (3), 216–222.